Mechanism of Additive-Assisted Room-Temperature-Processing of Metal-Halide Perovskite Thin Films

*Maged Abdelsamie [1,2], Tianyang Li [3], Finn Babbe [4], Junwei Xu [1], Qiwei Han[5], Volker Blum [3,5], Carolin M. Sutter-Fella [4], David B. Mitzi [3,5], Michael F. Toney [1, 6]**

[1]Stanford Synchrotron Radiation Light Source, SLAC National Accelerator Laboratory, Stanford University, Menlo Park, CA, USA

[2]Materials Sciences Division, Lawrence Berkeley National Laboratory, Berkeley, CA, USA

[3]Department of Mechanical Engineering and Materials Science, Duke University, Durham, NC, USA

[4]Chemical Sciences Division, Lawrence Berkeley National Laboratory, Berkeley, CA, USA

[5]Department of Chemistry, Duke University, Durham, NC, USA

[6]Department of Chemical and Biological Engineering, University of Colorado, Boulder, CO, USA

Department of Chemical and Biological Engineering
University of Colorado
Boulder, CO 80309, USA
Department of Chemical and Biological Engineering
University of Colorado
Boulder, CO 80309, USA
***E-mail:** michael.toney@colorado.edu

Keywords: Room-temperature-processing, additive engineering, halide perovskites, crystallization dynamics, film formation mechanism, precursor aggregates, in-situ GIWAXS, in-situ photoluminescence.

Abstract:

Perovskite solar cells have received substantial attention due to their potential for low-cost photovoltaic devices on flexible or rigid substrates. Thiocyanate (SCN)-containing additives, such as MASCN (MA = methylammonium), have been shown to control perovskite film crystallization and film microstructure to achieve effective room-temperature perovskite absorber processing. Nevertheless, the crystallization pathways and mechanisms of perovskite formation involved in MASCN-additive-processing are far from clear. Using *in situ* X-ray diffraction and photoluminescence, we investigate the crystallization pathways of $MAPbI_3$ and reveal the mechanisms of additive-assisted-perovskite formation, during spin coating and subsequent N_2-drying. We confirm that MASCN induces large precursor aggregates in solution and, during spin coating, promotes the formation of the perovskite phase with lower nucleation density and overall larger initial nuclei size, that form upon reaching supersaturation in solution, in addition to intermediate solvent-complex phases. Finally, during the subsequent N_2-drying, MASCN facilitates the dissociation of these precursor aggregates and the solvate phases, leading to further growth of the perovskite crystals. Our results show that the nature of the intermediate phases and their formation/dissociation kinetics determine the nucleation and growth of the perovskite phase, which subsequently impacts the film microstructure. These findings provide mechanistic insights underlying room-temperature, additive-assisted, perovskite-processing and help guide further development of such facile room-temperature synthesis routes.

Introduction:

Perovskite solar cells (PSCs) have made substantial advances in their photovoltaic performance, demonstrating efficiencies in excess of 25 % for single junction cells and 29 % for tandem-junction cells with silicon.[1–4] PSCs are considered the most promising next-generation solar cell technology due to several advantages, including superior performance, compatibility with cost-effective solution-processing using scalable techniques, and tunable

optoelectronic properties for applications in both single-junction and tandem solar cells. Several processing techniques have been effectively used to tune their microstructure, optoelectronic properties, stability, and functionality. Thermal annealing is frequently used to synthesize the most efficient perovskite solar cells by controlling perovskite crystallization through removal of excess solvent and enabling thermally-induced crystallization and grain growth.[4–7] However, thermal annealing has potential disadvantages that can limit the application of perovskites in flexible devices and tandem solar cells.[7–9] For instance, thermal annealing may induce detrimental interfacial reactivity with adjacent device structure layers (e.g., with the electron or hole transport layers).[10] For more complex device structures such as quantum dot (QD)/perovskite or all-perovskite tandem solar cells, high-temperature annealing can affect the previously deposited layers leading to their degradation.[11–13] Moreover, thermal annealing adds additional energy input, processing time and cost to PSC fabrication and limits the compatibility of the fabrication with roll-to-roll processing due to the need for large furnaces and longer annealing times.[14–16] To overcome the disadvantages of thermal annealing, several room-temperature approaches have been developed, including post-deposition anti-solvent dipping, two-step sequential deposition methods, pyridine (Py)-promoted perovskite formation, ligand-promoted perovskite formation from nanostructured precursors, and thiocyanate-based additive processing.[17–26] Nevertheless, many of these techniques involve two steps (such as dipping in a solvent, antisolvent or a precursor solution), which can alter the pre-deposited layers, making these techniques less compatible with complex device structures. Therefore, room-temperature processing techniques that involve a single solution processing step, such as thiocyanate additive-based processing, have a distinct advantage for applications over a wide range of device structures.[25,26]

Beyond thiocyanate-based approaches, numerous additives have been proposed in literature to tune the perovskite microstructure, including inorganic halide salts[27], organic halide salts[28], all-organic salts[29], polymers[30], fullerenes[31], small molecules[32], nanoparticles[33], solvent-additives[34], and acids[35]. Several different mechanisms for additive impact on film formation have been proposed, including additives acting as sites for heterogeneous nucleation, controlling the kinetics of crystal growth, coordinating with solutes (e.g. by hydrogen bonding with organic cations and/or chelating with lead ions), forming crystallized intermediate phases, and controlling the solubility of precursor solutes.[36,37] Nevertheless, most of these additives require a post-deposition thermal annealing treatment for effective conversion into high-performance perovskite films. Only a few additives such as thiocyanate-based additives have shown success in controlling perovskite film microstructure without requiring subsequent thermal annealing.[18,23,25] Notably, $Pb(SCN)_2$ has been used as an additive to control crystallization and manipulate perovskite film microstructure at room temperature in $MAPbI_3$-based and mixed cation mixed halide [$(Cs, FA, MA)Pb(Br,I)_3$, FA = formamidinium and MA = methylammonium] perovskite films.[26] Additionally, we have reported high-quality $MAPbI_3$ films with micron-sized grains, which were obtained using room-temperature MASCN-additive-processing.[25] We have shown that employing MASCN-additive-processing helps to obtain high-quality $MAPbI_3$ films with micron-sized grains and microsecond-range carrier lifetimes.[25] Solar cell devices employing such films exhibited high power conversion efficiency (PCE) of 18.22% with improved current–voltage hysteresis and good environmental stability over 1000 hours.[25] However, the mechanism of room-temperature additive-assisted perovskite film formation is still far from clear. An understanding of these mechanisms will provide facile and reproducible control of perovskite film microstructure.

In this work, we investigate the impact of the additive MASCN on $MAPbI_3$ perovskite formation during spin coating, with the dropping of an antisolvent

and subsequent N_2-drying, using *in situ* time-resolved grazing incidence wide-angle X-ray scattering (GIWAXS) and photoluminescence (PL). We show the formation of intermediate solvent-complexes and that the nature of these intermediate phases and their formation/dissociation kinetics impact the nucleation and growth of the $MAPbI_3$ perovskite phase, which affects the film microstructure. We show that MASCN induces large precursor aggregates in solution, giving rise to lower nucleation density for crystallization during spin coating. A $(MA)_2Pb_3I_8$.2DMSO intermediate phase is obtained in the as-cast film for the MASCN-free films, whereas an additional, but unidentified phase is obtained when adding MASCN to the precursor solution. The addition of MASCN to the precursor solution further facilitates the formation of the perovskite phase compared with the MASCN-free precursor. During the subsequent drying, the presence of MASCN in the wet film helps to dissociate the intermediate solvent-complexes, leading to the growth of perovskite phase into micron size crystals.

1. Experimental Section:

Perovskite preparation:

The $MAPbI_3$ perovskite thin films were deposited from a stoichiometric solution containing MAI [Sigma-Aldrich] and PbI_2 [Alfa-Aesar] with a concentration of 1.25 M. For the MASCN-samples, 50% MASCN and 5% extra PbI_2 were added to the precursor (both are mol% relative to $MAPbI_3$). For the additive-free samples, 5% extra PbI_2 was added to the precursor. The additional PbI_2 has been shown to improve device performance and was therefore added to both samples.[38–40] The precursor was dissolved in a mixture of anhydrous N,N-dimethylformamide (DMF) [Sigma-Aldrich] and dimethyl sulfoxide (DMSO) [Sigma-Aldrich] with a volume ratio of [DMF: DMSO = 9:1] at room temperature. The solution was filtered with a 0.2 µm PTFE filter prior deposition. Perovskite films were spin-coated on conventional static spin-coating, where the precursor solution was loaded

and fully wetted on the glass substrate before starting the spin-coating process. The glass substrates were cleaned with acetone and isopropanol, and then UV ozone treated for 20 min prior perovskite deposition. The spin-coating recipe is adopted from our previous work.[25] Spin coating was performed at a spin speed of 5000 rpm for 30 s, while an anti-solvent (chlorobenzene [CB]) (about 150 µl of CB per film) was applied 5 s after the start of the spin coating. The CB dropping was applied at a rate of 75 µL/s using an automated pump and a pipette, where the pipette tip outlet was placed 30 mm above the sample. To dry the wet film, a N_2 gas jet was blown onto the samples after spin coating. While the samples were dried using a low-vacuum treatment in our previous work,[25] the N_2-jet flow was used instead of the low-vacuum treatment in this work due to the technical difficulties of performing the in situ X-ray measurements in a vacuum chamber. The N_2 gas jet was blown onto the samples through a tube with 4 mm internal diameter placed at 30 mm above the substrate, where the flow was adjusted using a pressure gauge (adjusted to 3 pounds per square inch (PSI) relative to atmospheric pressure).

***Grazing incidence wide-angle X-ray scattering (GIWAXS)**:*

GIWAXS was performed at the Stanford Synchrotron Radiation Lightsource (SSRL). An incident angle of 1-2° was used to ensure obtaining scattering from the bulk of the thin film. Data processing was performed using the Nika software package for Wavemetrics Igor,[41] in combination with WAXStools,[42] with a custom written Igor script. In situ GIWAXS during spin coating and subsequent N_2 drying was performed at beamline 7-2 at an X-ray energy of 14 keV using a time resolution of 0.2 s. A Dectris Pilatus 300K detector in portrait mode was used to collect the scattered X-rays. The sample-to-detector distance was calibrated using a LaB_6 standard and was 383.1 mm. Our spin coater is contained in a custom-made chamber with inert environment for the in situ GIWAXS experiments to ensure no exposure to moisture or oxygen, as previously reported in Abdelsamie et al. (2020).[43]

After spin coating, the setup was adjusted for the N_2-drying treatment within ~ 1-2 min after spin coating. Some GIWAXS measurements were obtained at beamline 11-3 at an X-ray energy of 12.7 keV with acquisition time of 30 s per measurement.

In situ photoluminescence (PL):

In situ PL measurements were performed on a custom-made confocal setup at the Lawrence Berkeley National Laboratory in an inert atmosphere (N_2) glove-box as described in previous works.[44,45] Excitation was performed using a 532 nm laser diode, whereas the PL emission was collected using a fiber coupled with an Ocean Optics spectrometer (Flame) calibrated by the manufacturer. A maximum power density of ~30 mW-cm^{-2} was used during in situ PL measurements. PL emission signals were fitted using single Gaussian peak fitting after Jacobian-correction and linear background removal.[46] We note that, for *in situ* PL measurements, the N_2 gas jet was blown onto the samples using a N_2 gun, where the N_2-drying treatment was applied within ~15 s after spin coating. The noise in the PL results in section 2.4 can be attributed to the vibration induced by the N_2 circulation in the glovebox, where N_2 was pumped into the glove-box frequently every 30-40 s. This noise is more significant for the PL experiments of the stationary samples during the N_2 drying as compared to the PL experiments during spin coating where the PL signal is averaged over an area of the sample.

Solution small-angle X-ray scattering (SAXS):

Solution SAXS was collected at beamline 4–2 at the SSRL. The solution sample was contained in a quartz capillary tube with a 1 mm diameter and 0.1 mm wall thickness, purchased from the Charles Supper Company, Inc. An X-ray energy of 15 keV was used, with a sample-detector distance of 3.5 m. A Pilatus 1M fast detector was used to collect the scattered x-rays.

Scattering background from pure solvents (DMF: DMSO [9:1]) was acquired and subtracted from the precursor solution SAXS profiles.

Polarized optical microscopy (POM):

POM images were collected using a Nikon LV100 POL microscope with 100x magnification.

Scanning electron microscopy (SEM):

SEM images were collected using Quanta FEG 250 with an electron beam acceleration of 10 kV.

2. Results and discussion:

We first reveal the impact of MASCN on the microstructure of the as-cast and N_2-dried films. Then, we demonstrate the roles of MASCN in film formation in three stages: the solution stage (I), the spin coating stage (II), and the N_2-drying stage (III). We finally provide a summary of the mechanism of MASCN in controlling the film formation and tuning the film microstructure.

2.1 Role of MASCN in intermediate phase formation: GIWAXS of thin films

To reveal the role of MASCN in the crystallization of perovskite films, we have performed GIWAXS measurements on the as-cast and N_2-dried films coated from solutions containing 50% MASCN and MASCN-free precursors in 9:1 DMF:DMSO with an additional 5% PbI_2, added since this has been shown to improve the perovskite solar cell performance.[25,39] GIWAXS images of the as-cast and dried thin films are shown in **Figure 1** and show weakly textured X-ray scattering. Hence, we show the integrated scattering intensities as intensity vs scattering vector in **Figure 2**a. As shown in **Figure 1**a&c and **Figure 2**, the as-cast films exhibit the presence of ordered intermediates,

and additional peaks appear for the films with MASCN that are absent from the films without MASCN. For the films without MASCN, intermediate phase peaks at $q \approx 0.47$, 0.51, 0.65, 0.83, and 0.92 $Å^{-1}$ match with the known DMSO-intermediate solvate phase with a composition of $(MA)_2Pb_3I_8 \cdot 2DMSO$ (**Figure 1**a and **Figure 2**a).[47,48] Since the $(MA)_2Pb_3I_8 \cdot 2DMSO$ phase contains MAI:PbI_2 with molar ratio of 2:3, an excess of MAI presumably exists in the material surrounding the $(MA)_2Pb_3I_8 \cdot 2DMSO$ phase in the as-cast wet film. Given that no other diffraction peaks are observed, this excess MAI must be incorporated within an amorphous phase, with the possibility of containing dissolved Pb^{2+} and I^- ions, and perhaps the solvents.

For the films with MASCN, additional peaks at $q \approx 0.25$, 0.55 and 0.72 $Å^{-1}$ reveal the presence of another distinct intermediate phase (**Figure 1**c and **Figure 2**a). Note that the scattering peak at $q \approx 0.25$ $Å^{-1}$ overlaps with scattering from the specular X-ray reflection from the substrate at $q \sim 0.26$-0.3 $Å^{-1}$, as observed in GIWAXS images of a bare glass substrate (**Figure S1**). However, the diffraction peaks from the intermediate phase can be differentiated from this reflection, as the scattering peak from the unknown phase appears as arc-like scattering (see **Figure 1**c) but the reflection feature only occurs near azimuthal angle $\chi = 0$ (see **Figure S1**). Importantly, a significant enhancement of the $(MA)_2Pb_3I_8 \cdot 2DMSO$ peak intensity was observed with relatively sharper peaks (i.e., smaller full width at half maximum [FWHM]) for the films with MASCN compared to the films without MASCN, showing the formation of larger average crystallite size. The additional unidentified peaks only appear for the MASCN-containing samples, showing that this intermediate phase very likely contains MASCN as well as possibly DMSO and DMF solvent molecules. We were unable to match these additional peaks to any known phases and to possible structures obtained from density functional theory as discussed in the Supporting Information.

We have also performed GIWAXS measurements on as-cast films coated from precursor solutions containing extra 50% MASCN and extra 5% PbI_2 in

pure DMF and pure DMSO, (see **Figure S2** and **Figure S3)**. Notably, the intermediate solvate phases $(MA)_2Pb_3I_8{\cdot}2DMF$ and $(MA)_2Pb_3I_8{\cdot}2DMSO$ appear in these films involving pure DMF and pure DMSO, respectively, but the unknown phase was not observed in films prepared from either of the pure solvents.[47–49] Excess MAI and MASCN exists in the material surrounding the crystalline phases within both of the wet as-cast films prepared from pure solvents. This is deduced because the crystalline solvate phases do not contain MASCN and stoichiometric calculations of the solvate phases imply MAI:PbI_2 with molar ratio of 2:3. Thus, MAI and MASCN must be present in an amorphous intermediate solvate phase that we cannot detect with GIWAXS. Based on this, for the MASCN-samples prepared from mixed DMF/DMSO, we expect that MASCN is present and partitioned between the unknown phase and an amorphous phase. We note that the presence of amorphous phases is frequently observed in the reaction pathways of metal halide perovskites.[43,48–51]

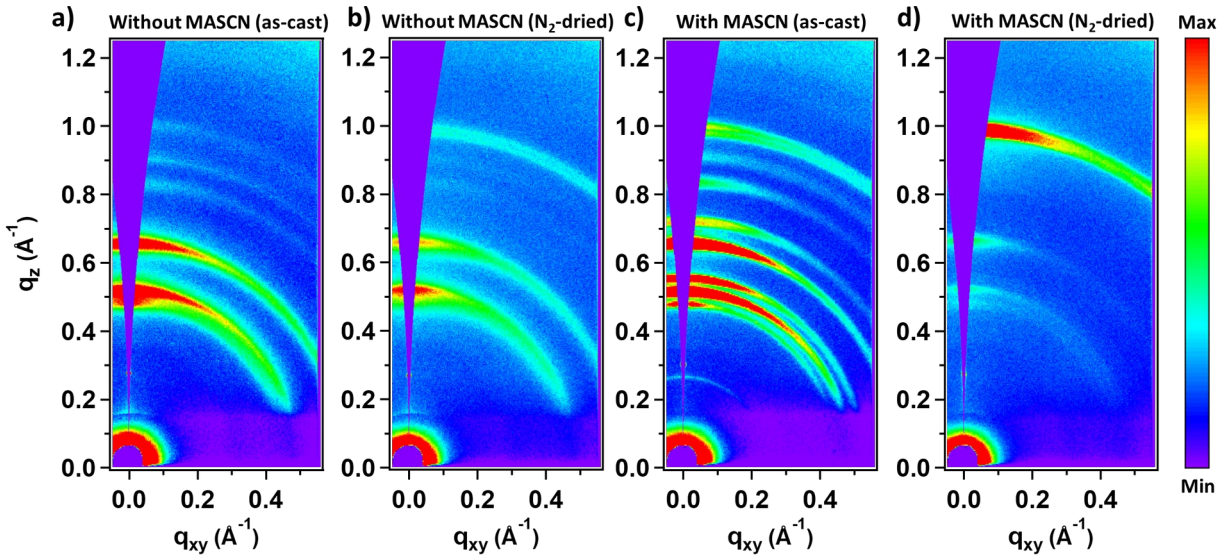

Figure 1 (a-b) GIWAXS plots of the as-cast and dried films prepared without MASCN; (a) as-cast (b) after N_2 drying. (c-d) GIWAXS plots of the as-cast and dried films prepared with MASCN; (c) as-cast and (d) after N_2 drying. The intensity scale bar is shown as a logarithmic color scale at the right. The

values of (min, max) are (310, 1250) for GIWAXS images in (a) and (b), and (310, 1600) for GIWAXS images in (c) and (d).

The as-cast films display the characteristics of a *sol–gel* process, as indicated by the presence of ordered intermediate phases containing DMSO, likely MASCN and possibly DMF.[52,53] We have applied a N_2 flow on the films to facilitate drying of the volatiles and to mimic the vacuum drying in our previous work.[25] GIWAXS images of the films after N_2 drying are shown in **Figure 1**b and d. For the samples without MASCN, very little conversion to $MAPbI_3$ perovskite occurs, as revealed by the weak development of the perovskite peak near $q \approx 1.0$ Å^{-1} (**Figure 1**b and the corresponding scattering intensity in **Figure 2**a). Correspondingly, only a small portion of the $(MA)_2Pb_3I_8$▪2DMSO phase dissociates, as seen by the relatively modest reduction of the $(MA)_2Pb_3I_8$▪2DMSO peaks. On the other hand, for the samples with MASCN, substantially more perovskite conversion occurs upon N_2 drying as revealed by the large increase in perovskite peak intensity and the significant reduction in intermediate phase peaks (**Figure 1**d and **Figure 2**a). For instance, the unknown phase associated with the peaks at $q \approx 0.25$, 0.55 and 0.72 Å^{-1} disappears completely and only a small amount of the $(MA)_2Pb_3I_8$▪2DMSO phase remains after N_2 drying. This comparison of samples shows that MASCN is of crucial importance for facile room temperature perovskite formation, consistent with our previous work.[25] To investigate the role of MASCN in the film microstructure, we have acquired polarized optical microscopy (POM) images and scanning electron microscopy (SEM) images for N_2-dried films prepared with and without MASCN (**Figure 2**b-e). From the POM images, the N_2-dried films prepared with MASCN exhibit micron-size features, whereas the N_2-dried films prepared without MASCN are featureless at the macroscale. SEM images confirm the formation of micron-size crystals for the N_2-dried films prepared with MASCN (**Figure 2**d). For the N_2-dried films prepared without MASCN (**Figure 2**e), we observe small grains surrounded by precursor material that we attribute to the non-complete

conversion of these films to the perovskite phase as observed by GIWAXS (**Figure 2**a). These results are consistent with our earlier work showing that MASCN promotes the room-temperature formation of micron-size perovskite grains.[25]

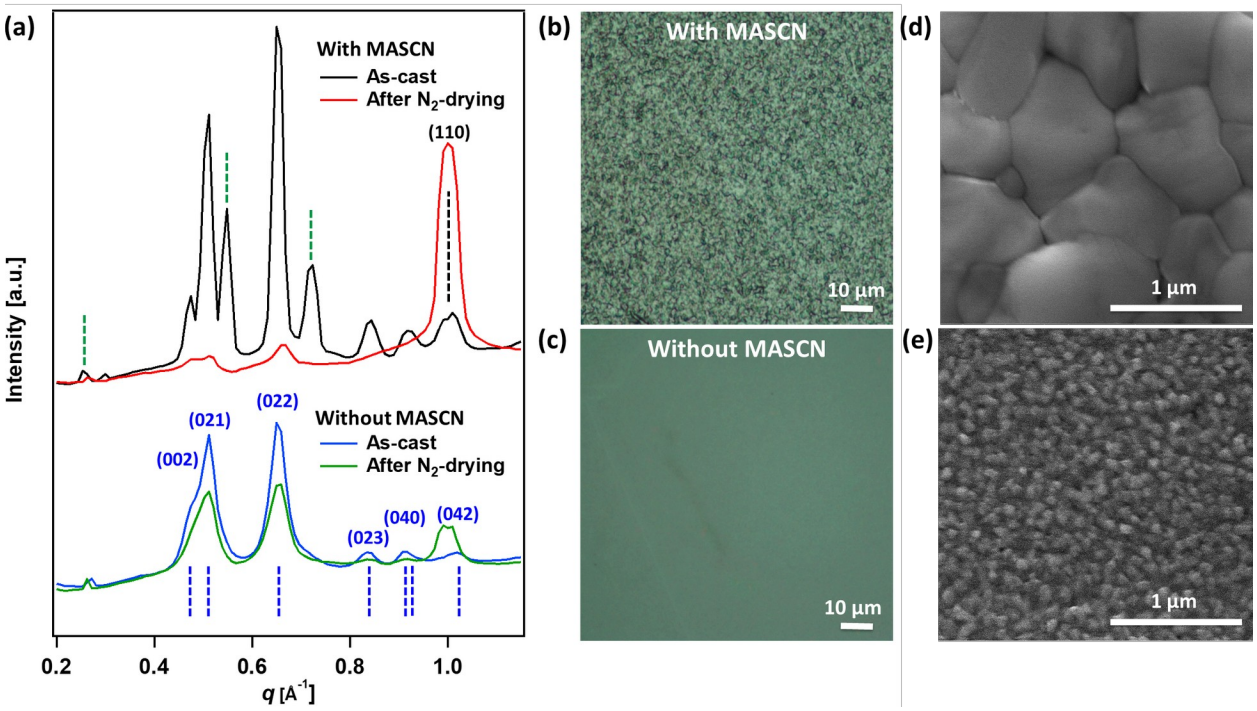

Figure 2 (a) Integrated scattering intensity of GIWAXS measurements of the as-cast sample prepared with MASCN (black), N_2-dried sample prepared with MASCN (red), the as-cast sample prepared without MASCN (blue), and N_2-dried sample prepared without MASCN (green). (b-c) POM images of the N_2-dried sample prepared with MASCN and without MASCN in (b) and (c), respectively. (d-e) SEM images of the N_2-dried sample prepared with MASCN and without MASCN in (d) and (e), respectively. The scattering intensities in (a) were integrated over the available polar angle on the detector. The as-cast measurements were taken at ~30 s after spin coating. The $MAPbI_3$ perovskite tetragonal (110)/(002) peak is labeled and marked by a black dashed line. $(MA)_2Pb_3I_8{\cdot}2DMSO$ solvate intermediate peaks are labeled and marked by blue dashed lines. The unknown phase peaks are marked by green dashed lines. There is scattering at low q (~ 0.26-0.3 $Å^{-1}$)

corresponding to an artifact from the reflected X-ray beam, which is observed as well for a bare glass sample (see **Figure S1**). Note that the scattering from the reflected X-ray beam partially overlaps with the unknown phase peaks.

2.2 Effect of MASCN on solution stage

To investigate the precursor aggregates in the initial solutions, we have performed solution SAXS on precursor solutions with and without MASCN (Figure 3). A significant increase in scattering at low q is observed for the precursor solution with 50% MASCN compared to MASCN-free solutions, indicating the formation of a higher concentration of larger precursor aggregates in the precursor solution with 50% MASCN. Due to the limited q range of the solution SAXS measurements, the size of aggregates cannot be estimated from this measurement. Nevertheless, in a previous work using dynamic light scattering (DLS), we showed that MASCN addition increases the precursor aggregate size from ~ 0.3 to 2.5 µm for 0 to 50% MASCN addition, respectively.[25] We propose that the formation of much larger aggregates in solutions containing MASCN is facilitated by the coordination of SCN^- ligands with PbI_x, which contributes to aggregate growth. Previous studies have shown that ligand-intermediates can reduce the activation energy for perovskite crystallization.[20,54] Therefore, we hypothesize that the presence of large aggregates reduces the activation barrier for the initial perovskite crystallization during film formation as discussed below.[20,54] Notably, previous studies suggest that the precursor aggregates exist as complex colloidal crystalline dispersions rather than simple colloidal structures such as amorphous colloids or undissolved lead iodide.[55,56]

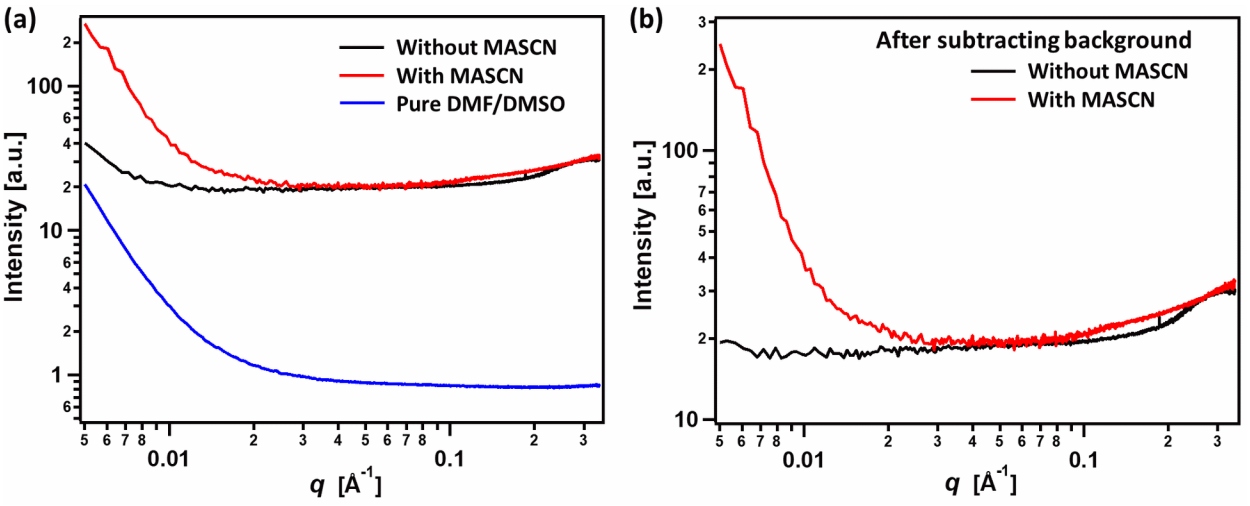

Figure 3 (a) Solution small-angle X-ray scattering (SAXS) profiles for pure DMF/DMSO (blue curve) and for $MAPbI_3$ precursor solution in DMF/DMSO with the addition of extra 5% PbI_2; without MASCN (black curve) and with 50% MASCN (red curve). (b) Solution SAXS profiles for 0% MASCN sample (black curve) and 50% MASCN sample (red curve) after subtracting the background using the scattering from pure DMF/DMSO sample.

2.3 In situ GIWAXS during film formation

To further examine the mechanism underlying MASCN impact in $MAPbI_3$ perovskite film formation, we have performed *in situ* GIWAXS during spin coating and subsequent N_2 drying of the $MAPbI_3$ precursor with and without MASCN. 2D false color plots of *in situ* GIWAXS measurements are shown in **Figure 4**a-b and **Figure 4**c-d for samples prepared with and without MASCN, respectively, whereas the time-evolution of integrated intensity of selected diffraction peaks appears in **Figure 5**a-b and **Figure 5**c-d for samples with and without MASCN, respectively. The anti-solvent (Chlorobenzene [CB]) was dropped after 5 s from the start of the spin coating, which has been shown to be crucial for obtaining high quality $MAPbI_3$ perovskite films.[25] For the MASCN-sample, a broad scattering from $q \sim 0.3$-0.7 $Å^{-1}$ (**Figure 4**a), corresponding to scattering from the bulk solvent (DMF and DMSO mixture), was observed at the beginning of the spin coating (see

Figure S1). Upon dropping CB at 5 s, the perovskite peak (at $q \approx 1.0$ Å^{-1}) develops immediately followed by a sharp increase of the $(MA)_2Pb_3I_8$·2DMSO peaks that occur shortly after ~6 s from the start of the spin coating (**Figure 4**a and **Figure 5**a). On the other hand, the unknown intermediate peak (at $q \approx 0.72$ Å^{-1}) associated with MASCN evolves more slowly after ~8 s of spin coating. It is worth noting that the perovskite phase decays slowly after 10 s. This evolution of the perovskite phase can be explained as the perovskite phase being unstable in the solvent rich environment, thus leading to slow decomposition into the intermediate phases. We attribute the crystallization of the perovskite phase upon dropping of CB for the MASCN sample to the MASCN-facilitated aggregates in the precursor solution (see Figure 3).

The as-cast film is swollen with DMSO and MASCN volatile compounds, requiring drying of these volatiles for further perovskite conversion. Notably, the formation of DMSO-intermediate complexes is more dominant compared to DMF-intermediate complexes in our films as DMF is more volatile and has weaker coordination with Pb^{2+} compared to DMSO, which is consistent with previous studies.[57] Therefore, we have used a N_2-flow approach to facilitate the evaporation of volatiles and resulting formation of the perovskite phase. As shown in **Figure 4**b and **Figure 5**b, upon applying N_2 flow, we observe decay in intermediate peaks and a simultaneous increase in perovskite peaks. Importantly, the two intermediate phases decay with different rates, which are associated with different stability. Looking closely at the decay rate of the intermediate peak at $q \approx 0.72$ Å^{-1} (the unknown phase) reveals that this phase disappears relatively quickly, as indicated by the diffraction peak decay within 2 min of applying N_2. Its disappearance is consistent with the idea that the unknown phase contains molecules/ions with higher volatility than $(MA)_2Pb_3I_8$.2DMSO phase (such as the highly volatile MASCN). On the other hand, the $(MA)_2Pb_3I_8$·2DMSO phase decays significantly more slowly and a portion of this phase remains in the film after N_2 drying. Notably, the perovskite phase growth during N_2-drying (**Figure 5**b) occurs in

two stages. In the first stage, significant conversion to perovskite phase (~80% of the final amount) occurs within the initial 2 min, with this stage associated with the nearly complete decay of the unknown phase and fast decay of $(MA)_2Pb_3I_8$.2DMSO phase (**Figure 5**b and **Figure S4**a). At the end of this stage, only a small amount of the unknown phase remains in the film. This stage is followed by a stage of slower conversion to the perovskite, which is associated with the slower loss of the $(MA)_2Pb_3I_8$·2DMSO phase (**Figure 5**b and **Figure S4**b).

In contrast, *in situ* GIWAXS during spin coating of the MASCN-free sample reveals the formation of the $(MA)_2Pb_3I_8$·2DMSO phase upon dropping of the anti-solvent CB, whereas the peaks from the unknown intermediate phase are absent, as shown in **Figure 4**c and **Figure 5c**. Moreover, we observe very little increase in GIWAXS integrated intensity from the perovskite peak at $q \approx 1.0$ Å^{-1}, in stark contrast to the MASCN-sample for which a sharp increase in this peak was observed (**Figure 5**a). During N_2 drying, a slow and steady decay of $(MA)_2Pb_3I_8$·2DMSO peaks proceeds, with concurrent increase in the perovskite peak ($q \approx 1.0$ Å^{-1}) (**Figure 4**d and **Figure 5**d). However, the $(MA)_2Pb_3I_8$·2DMSO decomposition is much slower compared to that for the MASCN-sample (see **Figure S4**), demonstrating that the presence of MASCN contributes to the more rapid loss of the $(MA)_2Pb_3I_8$·2DMSO phase in the MASCN-sample (**Figure S4**a and **Figure S5**a). This behavior is attributed to destabilization of the $(MA)_2Pb_3I_8$·2DMSO phase by MASCN, possibly through the interaction between $(MA)_2Pb_3I_8$·2DMSO and the surrounding matrix of SCN^{-1} within the film (expected, given 50% excess of this ion within the initial precursor solution). Note that some of the concentration of SCN^{-1} likely exists in the film in the form of an amorphous phase.

These results reveal that the presence of MASCN promotes precursor aggregation in solution, thus facilitating initial perovskite crystallization upon dropping antisolvent during spin-coating. As a reminder, this initial

crystallization happens before the gradual formation of the unknown phase in **Figure 4**a and **Figure 5**a and also prior to the vanishing of the unknown phase and formation of the final perovskite product in **Figure 4**b and **Figure 5**b. Previous studies have shown that lower nucleation density, when combined with faster crystal growth, results in larger crystal sizes.[58] Thus, we speculate that since the aggregates are larger (see **Figure 3**), these initial seed crystals have a lower density. As these initial low-density crystallites in the as-cast film seed the perovskite phase growth and the additives enhance the rate of crystal growth during subsequent drying (see **Figure 4**b), the resulting grain sizes are larger (see **Figure 2**b-e). These observations and hypothesis are consistent with a previous study in which the additive-induced larger aggregates in solution result in lower nucleation density and larger grains in 2D Ruddlesden–Popper perovskite thin films.[59]

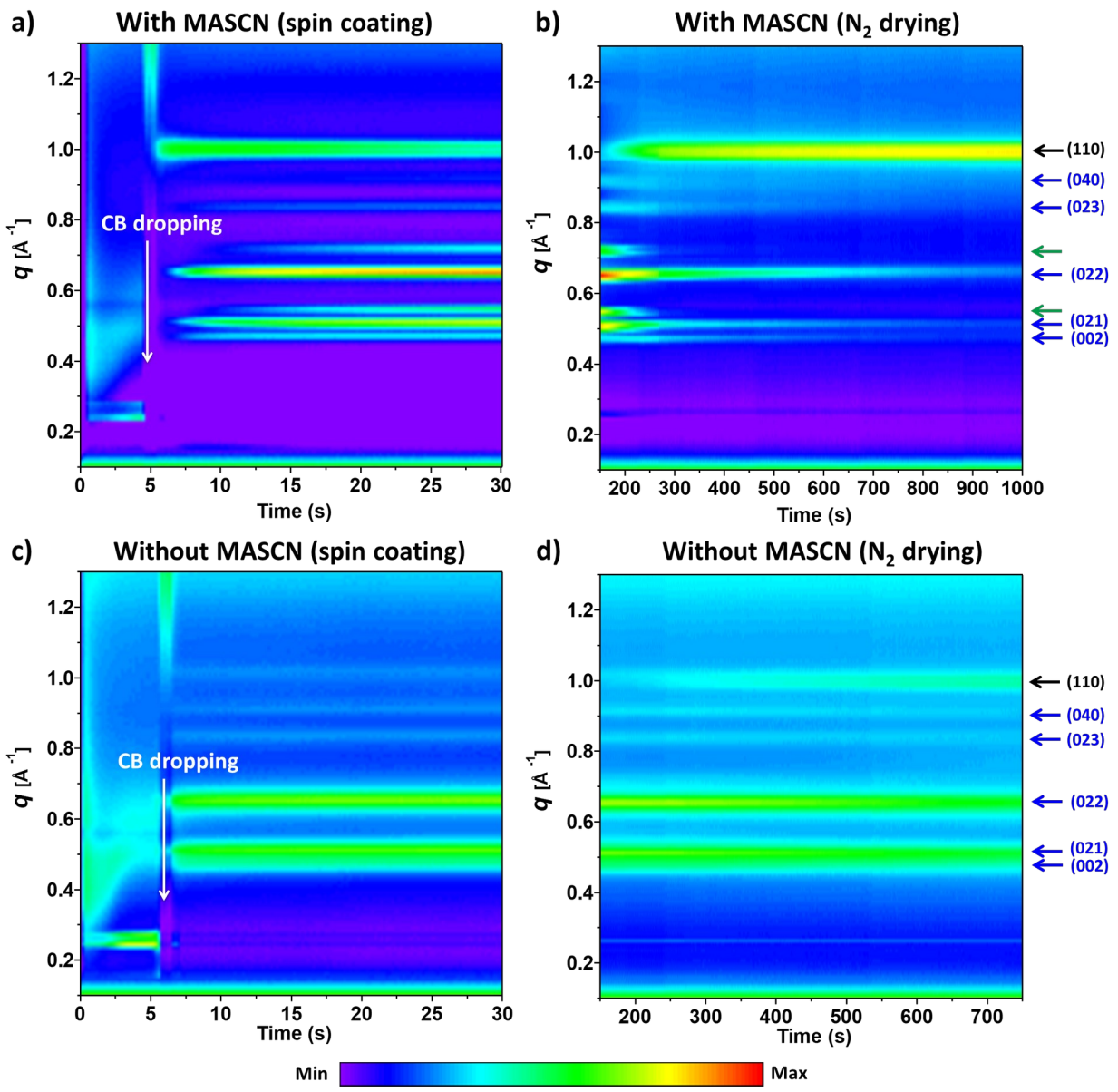

Figure 4 (a-b) Contour plots of in situ GIWAXS during film formation from $MAPbI_3$ precursor solution with 50% MASCN; (a) during spin coating and (b) during N_2 drying. (c-d) False-color plots of in situ GIWAXS during film formation from $MAPbI_3$ precursor solution without MASCN; (c) during spin coating and (d) during N_2 drying. CB dropping was applied after ~ 5 s from the start of the spin coating as marked by white arrow in (a) and (c). The $MAPbI_3$ perovskite (110)/(002) peak is marked by a black arrow. $(MA)_2Pb_3I_8{\cdot}2DMSO$ intermediate peaks are marked by blue arrows. The

unknown phase peaks are marked by green arrows. The intensity scale bar is shown as a logarithmic color scale at the bottom. The values of (min, max) are (310, 1600) for in situ GIWAXS images in (a) and (b), and (310, 1250) for in situ GIWAXS images in (c) and (d).

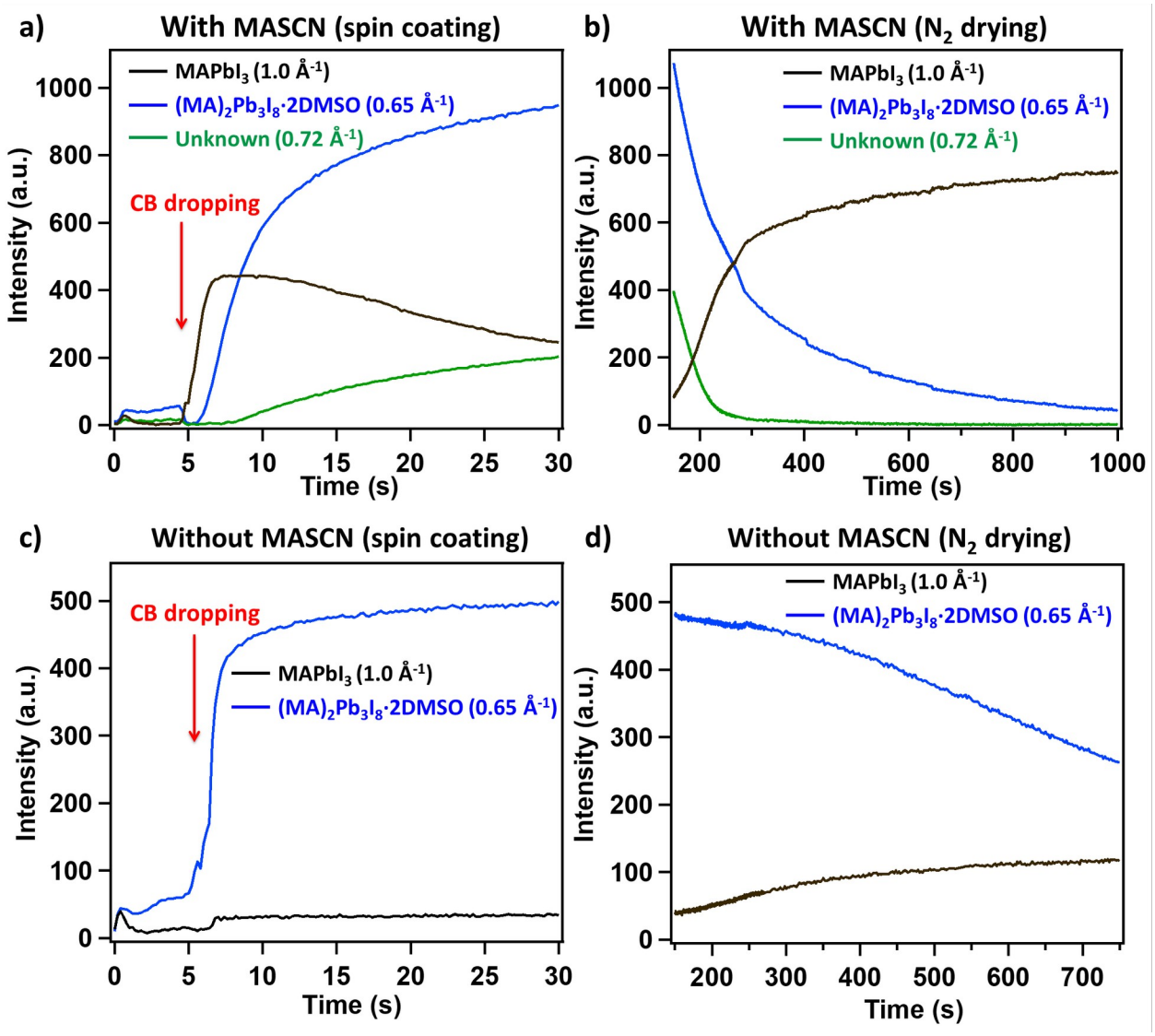

Figure 5 (a-b) Time evolution of the scattering intensities from selected diffraction peaks during film formation from $MAPbI_3$ precursor solution containing 50% MASCN; (a) during spin coating and (b) during N_2 drying. (c-d) Time evolution of the scattering intensities of selected diffraction peaks during film formation from $MAPbI_3$ precursor solution without MASCN; (c) during spin coating and (d) during N_2 drying. The evolution of perovskite

peak (q ≈ 1.0 $Å^{-1}$), $(MA)_2Pb_3I_8$·2DMSO peak (q ≈ 0.65 $Å^{-1}$), and the unknown phase peak (q ≈ 0.72 $Å^{-1}$) are shown in black, blue, and green, respectively. CB dropping was applied after ~ 5 s from the start of the spin coating as marked by the red arrow in (a) and (c). The scattering at q ≈ 0.65 $Å^{-1}$ at times < 5 s corresponds to the precursor solvent scattering that overlaps with the $(MA)_2Pb_3I_8$·2DMSO peak (blue curve).

2.4 In situ photoluminescence during film formation

To provide complementary information to the phase and structural evolution, *in situ* PL measurements were performed during the perovskite film formation. Relying on the high radiative recombination efficiency of $MAPbI_3$, *in situ* PL spectroscopy enables probing the nucleation and growth of $MAPbI_3$ crystals during film formation as demonstrated in previous studies.[44,45] Moreover, the strong PL signal is characteristic of the perovskite phase, not the intermediate phases.[44,60] We note that the dynamics of perovskite formation as measured by the *in situ* PL and GIWAXS should be discussed and compared qualitatively, as the two experiments were, of necessity, performed under different laboratory conditions. In case of the sample with MASCN, as shown in Figure 6a and **Figure 7**a, PL emission appears immediately upon dropping CB at ~ 5 s from the start of the spin coating. Importantly, the initial PL emission occurs at higher energies ~ 1.76 eV but rapidly shifts to ~ 1.64 eV within 2 s after dropping CB, accompanied by an order of magnitude increase in PL intensity. This is followed by a steady red shift of the PL peak to ~ 1.61 eV by the end of the spin coating, whereas the PL intensity stayed constant. The PL emission at higher energy can be attributed to nucleation of perovskite nanocrystals, where quantum confinement leads to higher PL emission energy.[44,45,61] The subsequent growth of $MAPbI_3$ crystals is reflected by the red shift in PL emission. The fast formation of $MAPbI_3$ indicated by the sharp evolution of PL emission is consistent with the *in situ* GIWAXS results where the perovskite phase peaks evolve immediately upon dropping CB (**Figure 4**a and **Figure 5**a). This

behavior can be facilitated by the presence of the large precursor aggregates in solution due to MASCN addition, as discussed above.[25] We anticipate that the precursor aggregates in solution act as nucleation sites for perovskite phase formation by reducing the activation barrier for perovskite crystallization.[20,54]

During the N_2 drying of the MASCN-sample (**Figure 6**b and **Figure 7**b), no significant changes were observed in the PL peak position or intensity. As discussed previously, the *in situ* GIWAXS during N_2 drying showed an increase in perovskite peaks at the expense of the unknown phase and the $(MA)_2Pb_3I_8{\cdot}2DMSO$ peaks (**Figure 4**b and **Figure 5**b). The increase in perovskite peak intensity can either be due to nucleation of additional perovskite crystals or the growth of existing crystals. Since the *in situ* PL measurements during N_2 drying do not show PL response at high PL energy, which can be associated with the nucleation of quantum-confined perovskite crystals, it is more likely that the N_2 drying promotes the growth of pre-existing perovskite crystals, consistent with the large grains observed.[62] Notably, the parameters influencing the PL intensity are manifold and it is not always easy to pinpoint what causes changes.[44,63] For instance, in a previous study, in situ PL measurements during thermal annealing of $MAPbI_3$ films have shown an increase in PL intensity during the initial crystallization followed by a decay in PL intensity during the subsequent growth of $MAPbI_3$ crystals, whereas the decay in PL intensity was linked to thermally induced effects and photodarkening.[44] It is noted, that both, the intensity increase and decrease were found to be dependent on the nature of the Pb-precursor.[44] In addition, an increase in PL intensity during thermal annealing performed in a fume hood was reported, which was linked to oxygen healing via the formation of a superoxide that passivates iodide vacancies.[64] For the observed stable PL intensity in our study, we anticipate that the growth of crystals can induce mechanisms that either increase or decrease the PL signal, whereas the observed stable PL intensity is possibly the result of two

mechanisms canceling out each other: 1. The crystal growth can reduce the density of the grain boundary which is quite defective and further reduce the number of bulk defects acting as recombination centers leading to an increase in PL signal. 2. A decrease in PL intensity during prolonged drying can be attributed to a change in optoelectronic properties such as a decrease in the net charge carrier (doping) density.[65] For instance, a decrease in PL quantum yield with prolonged annealing time was linked to an order of magnitude decrease in the net doping density rather than an increase in non-radiative recombination.[65] Such a decrease in net doping density was attributed to a decrease of Pb-vacancies with prolonged annealing time.[65] On the other hand, for the MASCN-free sample, no PL emission was observed upon dropping CB during spin coating (**Figure 6**c and **Figure 7**c). Nevertheless, a very broad and weak PL emission was observed at the end of spin coating (**Figure 6**c and **Figure S6**c). During N_2 drying, a steady increase in PL emission intensity is observed (**Figure 6**d and **Figure 7**d). The PL emission initially occurs at high energy centered at ~1.96 eV and with relatively broad spectra (with FWHM ~ 0.2 eV), shifting to ~ 1.76 eV (with FWHM ~ 0.1 eV) during the initial 100 s of N_2-drying (see **Figure 6**d, **Figure S6**d**,** and **Figure S7**d). We assign this initial stage of $MAPbI_3$-formation to that dominated by nucleation of small $MAPbI_3$ crystals. The delay in the appearance of PL emission indicates a delay in $MAPbI_3$ nucleation and formation. In addition, the extremely high initial emission energy suggests strong quantum confinement and formation of nanodomains.[62,66] Tuning of the semiconductor bandgap via quantum confined size effects is widely used in optoelectronic applications and has been reported for $MAPbI_3$ synthesized in nanoporous templates with a blue shift of up to 150 nm.[66,67] For instance, a study has reported a reduction in bandgap of $MAPbI_3$ confined nanocrystals in a nanoporous template from 1.75 to 1.62 eV with the increase in pore size from 5.1 to 11.9 nm, respectively.[67] The magnitude of the blue shift is not as pronounced for the MASCN-containing samples indicating a reduced quantum confinement effect

and consequently the initial formation of relatively larger nuclei size at the beginning of the nucleation during supersaturation of the precursor solution. The following gradual red shift to ~1.65 eV and simultaneous increase in PL intensity as well as decrease in FWHM to ~ 0.07 eV over the subsequent ~ 300 s of N_2 drying is ascribed to the growth of $MAPbI_3$ crystals (see **Figure 6**d, **Figure 7**d, and **Figure S7**d). The PL emission reaches steady state after 400 s of applying N_2 with very little subsequent change in both PL peak position and intensity. The slow and steady evolution of PL emission for the MASCN-free sample agrees with the *in situ* GIWAXS results, for which perovskite peak intensity increases with a slow rate, accompanied by slow dissociation of the $(MA)_2Pb_3I_8 \cdot 2DMSO$ phase.

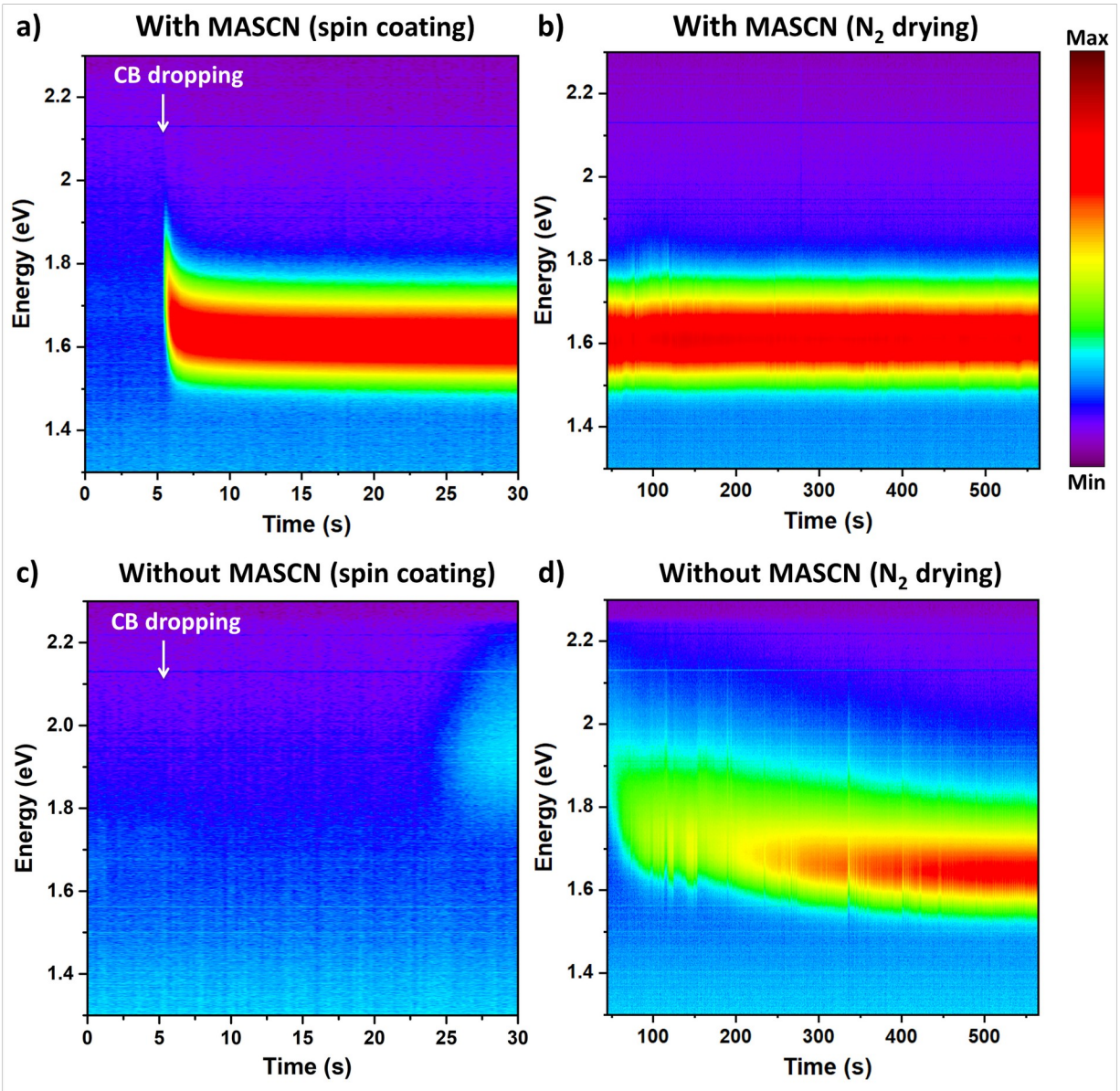

Figure 6 (a-b) Contour plots of *in situ* PL during film formation from $MAPbI_3$ precursor solution containing MASCN; (a) during spin coating and (b) during N_2 drying. (c-d) Contour plots of in situ PL during film formation from $MAPbI_3$ precursor solution without MASCN; (c) during spin coating and (d) during N_2 drying. CB dropping was applied after ~ 5 s from the start of the spin coating as marked by white arrow in (a) and (c).

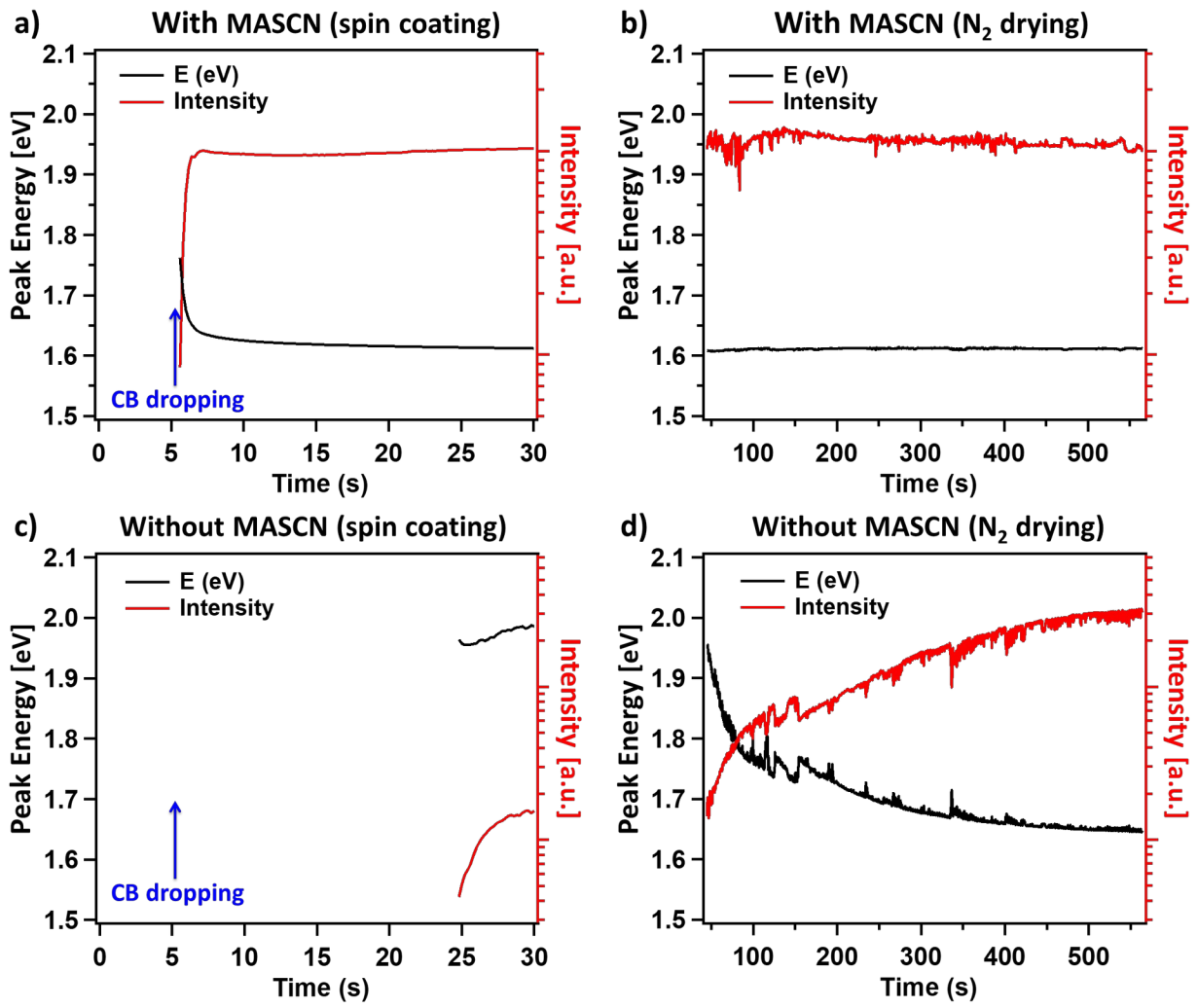

Figure 7 (a-b) Time-evolution of peak energy and intensity *of in situ* PL during film formation from $MAPbI_3$ precursor solution containing MASCN; (a) during spin coating and (b) during N_2 drying. (c-d) Time-evolution of peak energy and intensity of in situ PL during film formation from $MAPbI_3$ precursor solution without MASCN; (c) during spin coating and (d) during N_2 drying. CB dropping was applied after ~ 5 s from the start of the spin coating as marked by blue arrow in (a) and (c). The N_2 drying treatment was applied ~ 15 s after the conclusion of spin coating.

2.5 Mechanism of the perovskite formation

From the previous discussion, we can propose a mechanism for the effect of MASCN in the room temperature formation process of $MAPbI_3$ (**Figure 8**). The roles of MASCN can be summarized in three stages (that are discussed in detail below): the solution stage (I) with the formation of large aggregates in solution; the spin coating stage (II) with the formation of initial perovskite crystallites (due to large aggregates) as well as intermediate solvate phases upon dropping antisolvent prior to drying; and the drying stage (III) with the rapid dissociation of the intermediate phases and growth of large perovskite crystallites (due to low nucleation density) during room temperature drying treatment, which is facilitated by MASCN.

In stage (I), the addition of MASCN to the precursor solution promotes the formation of large precursor aggregates (possibly associated with SCN^- coordination with PbI_x) as compared to the MASCN-free solution (**Figure 8**a&c). In stage (II), initial perovskite crystallites form with sparse nucleation density (due to the large precursor aggregates) together with $(MA)_2Pb_3I_8$.2DMSO phase and an unknown phase (likely associated with MASCN and DMSO) upon antisolvent dropping during spin coating (**Figure 8**a). In a previous work,[25] we have shown a strong correlation between the aggregate size in solution induced by MASCN and the $MAPbI_3$ crystal size in the final film. Similar behavior was reported for the 2D Ruddlesden–Popper $BA_2MA_4Pb_5I_{16}$ perovskite films, where the precursor aggregation in solution induced by the addition of phenylethylammonium iodide (PEAI) favors the formation of large crystal grains of the perovskite.[59] This phenomenon was explained by the larger aggregates in solution, which result in lower nucleation site density and larger grains in the perovskite films.[59] Similarly, MASCN addition gives rise to lower density of nucleation sites of the crystalline perovskite phase in the as-cast films. The as-cast MASCN-sample is represented in **Figure 8**a (right schematic) as a coexistence of perovskite phase (represented as black crystals), $(MA)_2Pb_3I_8$·2DMSO phase (represented as blue crystals), the unknown phase (represented as green crystals), and an amorphous medium. Notably, the crystalline phases in the as-cast MASCN

samples have larger crystallites with lower nucleation density compared to the as-cast MASCN-free samples (**Figure 8**a&c). The presence of amorphous medium in the as-cast films has been reported previously for various perovskite materials.[43,48–51] We similarly assume the presence of an amorphous phase that contains dissolved ions in DMF/DMSO, such as MA^{+}, Pb^{+2}, I^{-}, and SCN^{-} (for the MASCN samples).

In stage (III), film formation during the N_2 drying of MASCN-containing samples is represented schematically in **Figure 8**b. Upon applying N_2 flow, the volatiles likely continuously evolve from the wet film-air interface since the N_2 jet is applied on the film top-surface. The removal of the volatiles from the top-surface is hypothesized to create a concentration gradient (including for MASCN) across the sol-gel wet film. Consequently, volatiles (including MA^{+} and SCN^{-} ions) migrate to the top-surface. The migration of the volatiles leads to an increase in diffusion of the ionic species within the sol-gel wet film relative to the MASCN-free film, thereby providing the kinetics for the growth of the perovskite crystals at room temperature.[68] Our hypothesis on the increase in the diffusion of the ionic species within the wet film is supported by the enhancement in the kinetics of perovskite phase crystallization and intermediate phases dissociation for the samples prepared with MASCN compared to samples prepared without MASCN. In addition, we speculate that the presence of MASCN in the sol-gel wet film may have effects on the thermodynamics of the existing phases in the film. The presence of MASCN in the sol-gel wet film destabilizes the $(MA)_2Pb_3I_8.2DMSO$ phase as shown by its faster decay compared to the MASCN-free sample (**Figure 5**b&d). We hypothesize that the interaction of intermediate phases with the volatiles (such as SCN^{-1}) destabilizes the intermediate phases leading to their facile dissociation. SCN^{-} likely reduces the interaction between octahedral Pb–I configurations (PbI_x) and DMSO by competing with DMSO for coordination sites with PbI_x (i.e., SCN^{-} coordinates strongly with PbI_x, thereby weakening the DMSO-PbI_x coordination).

The dissociation of the intermediate phases provides molecular species for either the growth of existing perovskite crystals or the nucleation and growth of additional crystallites. However, the nucleation of additional perovskite crystals during N_2 drying should give rise to PL emission at higher energy due to confinement, which was not observed (see **Figure 6**b). Additionally, the previously reported strong correlation between the size of the aggregates in solution and the grain size in thin films hints that the final microstructure is predominantly pinned by the density of perovskite nucleation sites induced by the aggregates size in solution, as noted above.[25] This correlation also suggests that there is likely no significant second nucleation event during N_2 drying, as this would reduce the final grain size. Therefore, during N_2 drying, the growth of existing perovskite crystals from the dissociated intermediate phases is likely more dominant than the nucleation and growth of new perovskite crystals, as represented schematically in **Figure 8**b. A schematic for a possible reaction pathway for perovskite phase growth at the expense of the $(MA)_2Pb_3I_8{\cdot}2DMSO$ and amorphous intermediate phases is shown in **Figure 9**. The presence of MASCN molecular species in the sol-gel wet film helps to dissociate the intermediate $(MA)_2Pb_3I_8{\cdot}2DMSO$ phase, which in turn, in combination with MAI from the amorphous phase, contribute to the growth of $MAPbI_3$ grains, as represented by the reaction in **Figure 9**. Here, the amorphous phase mediates the molecular diffusion of ionic species from the intermediate phases to the perovskite phase. Nevertheless, it is difficult to predict any specific reaction pathway that involves the unknown phase due to its unknown composition. Notably, the main role of MASCN is to manipulate the $MAPI_3$ crystallization during film formation whereas MASCN leaves the film during film drying. In a previous work, using depth-profiling X-ray photoelectron spectroscopy (XPS), we have shown the complete removal of MASCN in the dried films which was evidenced by the absence of any detectable residual sulfur within the dried films.[25]

For the MASCN-free samples (**Figure 8**c), dropping the antisolvent during spin coating gives rise to the formation of the $(MA)_2Pb_3I_8$·2DMSO phase with relatively smaller crystal sizes as revealed by the weaker and broader scattering peaks (**Figure 2**a). The as-cast MASCN-free sample is represented in **Figure 8**c (right schematic) as a combination of the $(MA)_2Pb_3I_8$·2DMSO phase (represented as blue crystals) and an amorphous medium. Here, due to the presence of smaller aggregates in solution, the nucleation density for crystallization is expected to be relatively higher than the MASCN-sample (**Figure 8**a&c). The film formation during subsequent N_2 drying for MASCN-free samples is represented schematically in **Figure 8**d. During N_2-drying, the $(MA)_2Pb_3I_8$·2DMSO phase dissociates relatively slowly, giving rise to the nucleation and growth of perovskite crystals, as evidenced by the PL emission at high energies, a characteristic of confinement of small perovskite crystals, during the initial 400 s of N_2-drying. As mentioned above, the N_2-drying at room temperature in the absence of MASCN is not sufficient for completing the perovskite formation and $(MA)_2Pb_3I_8$·2DMSO dissociation on the probed time scale. Typically, thermal annealing at elevated temperatures (*ca.* ≥ 90 ^{o}C) is required for additive-free-processing of $MAPbI_3$ films.[60,69]

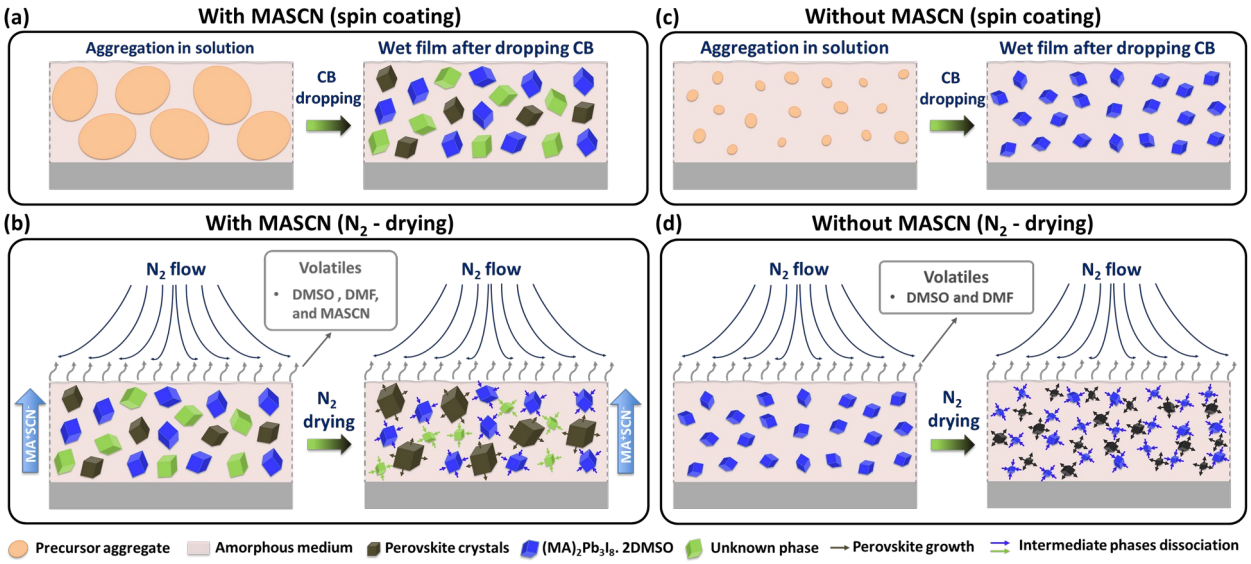

Figure 8 (a-b) Schematic represents the mechanism of film formation during spin-coating (a) and the subsequent N_2 drying (b) for $MAPbI_3$ precursor

solution with MASCN. (c-d) Schematic represents the mechanism of film formation during spin-coating (c) and the subsequent N_2 drying (d) for $MAPbI_3$ precursor solution without MASCN.

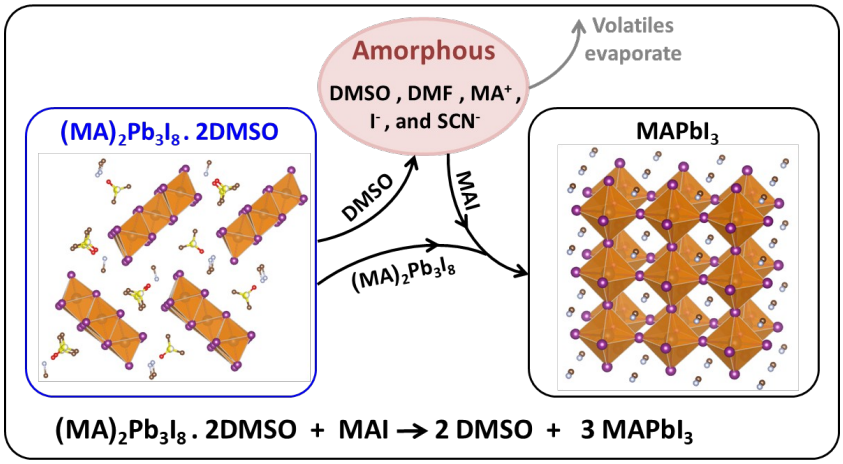

Figure 9 Schematic representation of the reaction pathway for the growth of perovskite at the expense of the $(MA)_2Pb_3I_8{\cdot}2DMSO$ and amorphous phases. The proposed reaction is shown on the bottom of **Figure 9**. The presence of SCN^- helps to dissociate $(MA)_2Pb_3I_8{\cdot}2DMSO$ at room temperature favoring the forward reaction (left-to-right), thus promoting perovskite crystallization. We propose that MA (= $CH_3NH_3^+$) and SCN^- react forming gases (CH_3NH_2 + HSCN) or (CH_3SCN + NH_3).[25,70] The volatiles diffuse to the air-film interface and evaporate.

3. Conclusion

In summary, we have investigated the dynamics of room-temperature perovskite formation during spin coating and subsequent N_2-drying and revealed the roles of an MASCN additive and its mechanism in perovskite formation. Time-resolved monitoring of perovskite film processing reveals the formation of intermediate phases during the sol-gel pathway to perovskite crystal formation. The nature of the intermediate phases and their formation/dissociation dynamics impact the extent of nucleation and growth of the perovskite phase and affect the microstructure of the perovskite film.

The addition of MASCN induces large precursor aggregates in solution, which promote perovskite crystallization, in addition to intermediate phases ($(MA)_2Pb_3I_8$·2DMSO and an unidentified phase) upon dropping an antisolvent during spin coating. During the subsequent N_2-drying, MASCN facilitates the dissociation of the intermediate phases leading to further growth of the perovskite crystals. We hypothesize that the larger aggregates in solution induced by MASCN limit the nucleation density of the initial perovskite crystallites during spin coating. Additionally, the high volatility of MASCN facilitates diffusion of MA^+ and SCN^- out of the sol-gel wet film, leading to an increase in the mass transport of the ionic species within the film, which is essential for perovskite crystal growth at room temperature. For the MASCN-free films, mainly the intermediate phase $(MA)_2Pb_3I_8$·2DMSO is obtained upon dropping the antisolvent during spin coating. During N_2-drying, partial perovskite phase formation occurs at the expense of some $(MA)_2Pb_3I_8$·2DMSO dissociation, indicating that this MASCN-free processing is less effective in fabricating well-formed perovskite films at room temperature. Our results provide a better understanding of the mechanism of room-temperature additive processing and can guide development of methods for enhanced control of perovskite formation.

4. Acknowledgements:

This work was wholly supported by the Center for Hybrid Organic-Inorganic Semiconductors for Energy (CHOISE), an Energy Frontier Research Center funded by the Office of Basic Energy Sciences, an office of science within the US Department of Energy (DOE) through contract number DE-AC36-08G028308. Use of the Stanford Synchrotron Radiation Light source (SSRL), SLAC National Accelerator Laboratory, is supported by the US DOE, Office of Science, Office of Basic Energy Sciences under Contract DE-AC02-76SF00515. *In situ* PL measurements were supported by the Joint Center for Artificial Photosynthesis, a DOE Energy Innovation Hub, supported through the Office of Science of the U.S. Department of Energy under Award Number

DE-SC0004993 (F.B.) and the Laboratory Directed Research and Development (LDRD) program of Lawrence Berkeley National Laboratory under U.S. Department of Energy contract number DE-AC02-05CH11231 (C.M.S.-F.).

5. Conflict of Interest:

The authors declare no conflict of interest.

6. Supporting information:

- GIWAXS of $MAPbI_3$ thin films prepared from precursors in different solvents, time-evolution of GIWAXS integrated intensities and PL spectra during the formation of $MAPbI_3$ thin films, and density-functional theory (DFT) investigation of the local stability of intermediate phase $(MA)_2Pb_3I_8 \cdot 2DMSO$.

7. References:

(1) Bush, K. A.; Palmstrom, A. F.; Yu, Z. J.; Boccard, M.; Cheacharoen, R.; Mailoa, J. P.; McMeekin, D. P.; Hoye, R. L. Z.; Bailie, C. D.; Leijtens, T.; Peters, I. M.; Minichetti, M. C.; Rolston, N.; Prasanna, R.; Sofia, S.; Harwood, D.; Ma, W.; Moghadam, F.; Snaith, H. J.; Buonassisi, T.; Holman, Z. C.; Bent, S. F.; McGehee, M. D. 23.6%-Efficient Monolithic Perovskite/Silicon Tandem Solar Cells with Improved Stability. *Nat. Energy* **2017**, *2* (4), 17009. https://doi.org/10.1038/nenergy.2017.9.

(2) Nayak, P. K.; Mahesh, S.; Snaith, H. J.; Cahen, D. Photovoltaic Solar Cell Technologies: Analysing the State of the Art. *Nat. Rev. Mater.* **2019**, *4* (4), 269–285. https://doi.org/10.1038/s41578-019-0097-0.

(3) Best Research-Cell Efficiency Chart | Photovoltaic Research | NREL https://www.nrel.gov/pv/cell-efficiency.html (accessed Feb 14, 2021).

(4) Green, M. A.; Ho-Baillie, A.; Snaith, H. J. The Emergence of Perovskite Solar Cells. *Nat. Photonics* **2014**, *8* (7), 506–514. https://doi.org/10.1038/nphoton.2014.134.

(5) Dubey, A.; Adhikari, N.; Mabrouk, S.; Wu, F.; Chen, K.; Yang, S.; Qiao, Q. A Strategic Review on Processing Routes towards Highly Efficient Perovskite Solar Cells. *J. Mater. Chem. A* **2018**, *6* (6), 2406–2431. https://doi.org/10.1039/C7TA08277K.

(6) Tai, Q.; Tang, K.-C.; Yan, F. Recent Progress of Inorganic Perovskite Solar Cells. *Energy Environ. Sci.* **2019**, *12* (8), 2375–2405. https://doi.org/10.1039/C9EE01479A.

(7) Berry, J.; Buonassisi, T.; Egger, D. A.; Hodes, G.; Kronik, L.; Loo, Y.-L.; Lubomirsky, I.; Marder, S. R.; Mastai, Y.; Miller, J. S.; Mitzi, D. B.; Paz, Y.; Rappe, A. M.; Riess, I.; Rybtchinski, B.; Stafsudd, O.; Stevanovic, V.; Toney, M. F.; Zitoun, D.; Kahn, A.; Ginley, D.; Cahen, D. Hybrid Organic–Inorganic

Perovskites (HOIPs): Opportunities and Challenges. *Adv. Mater.* **2015**, *27* (35), 5102–5112. https://doi.org/10.1002/adma.201502294.
(8) Fu, F.; Feurer, T.; Jäger, T.; Avancini, E.; Bissig, B.; Yoon, S.; Buecheler, S.; Tiwari, A. N. Low-Temperature-Processed Efficient Semi-Transparent Planar Perovskite Solar Cells for Bifacial and Tandem Applications. *Nat. Commun.* **2015**, *6* (1), 8932. https://doi.org/10.1038/ncomms9932.
(9) Chen, C.-C.; Bae, S.-H.; Chang, W.-H.; Hong, Z.; Li, G.; Chen, Q.; Zhou, H.; Yang, Y. Perovskite/Polymer Monolithic Hybrid Tandem Solar Cells Utilizing a Low-Temperature, Full Solution Process. *Mater. Horiz.* **2015**, *2* (2), 203–211. https://doi.org/10.1039/C4MH00237G.
(10) Dunlap-Shohl, W. A.; Li, T.; Mitzi, D. B. Interfacial Effects during Rapid Lamination within MAPbI3 Thin Films and Solar Cells. *ACS Appl. Energy Mater.* **2019**, *2* (7), 5083–5093. https://doi.org/10.1021/acsaem.9b00747.
(11) Zhang, Y.; Gu, M.; Li, N.; Xu, Y.; Ling, X.; Wang, Y.; Zhou, S.; Li, F.; Yang, F.; Ji, K.; Yuan, J.; Ma, W. Realizing Solution-Processed Monolithic PbS QDs/Perovskite Tandem Solar Cells with High UV Stability. *J. Mater. Chem. A* **2018**, *6* (48), 24693–24701. https://doi.org/10.1039/C8TA09164A.
(12) Palmstrom, A. F.; Eperon, G. E.; Leijtens, T.; Prasanna, R.; Habisreutinger, S. N.; Nemeth, W.; Gaulding, E. A.; Dunfield, S. P.; Reese, M.; Nanayakkara, S.; Moot, T.; Werner, J.; Liu, J.; To, B.; Christensen, S. T.; McGehee, M. D.; van Hest, M. F. A. M.; Luther, J. M.; Berry, J. J.; Moore, D. T. Enabling Flexible All-Perovskite Tandem Solar Cells. *Joule* **2019**, *3* (9), 2193–2204. https://doi.org/10.1016/j.joule.2019.05.009.
(13) Lin, R.; Xiao, K.; Qin, Z.; Han, Q.; Zhang, C.; Wei, M.; Saidaminov, M. I.; Gao, Y.; Xu, J.; Xiao, M.; Li, A.; Zhu, J.; Sargent, E. H.; Tan, H. Monolithic All-Perovskite Tandem Solar Cells with 24.8% Efficiency Exploiting Comproportionation to Suppress Sn(Ii) Oxidation in Precursor Ink. *Nat. Energy* **2019**, *4* (10), 864–873. https://doi.org/10.1038/s41560-019-0466-3.
(14) Li, H.; Zuo, C.; Scully, A. D.; Angmo, D.; Yang, J.; Gao, M. Recent Progress towards Roll-to-Roll Manufacturing of Perovskite Solar Cells Using Slot-Die Processing. *Flex. Print. Electron.* **2020**, *5* (1), 014006. https://doi.org/10.1088/2058-8585/ab639e.
(15) Ankireddy, K.; Ghahremani, A. H.; Martin, B.; Gupta, G.; Druffel, T. Rapid Thermal Annealing of CH3NH3PbI3 Perovskite Thin Films by Intense Pulsed Light with Aid of Diiodomethane Additive. *J. Mater. Chem. A* **2018**, *6* (20), 9378–9383. https://doi.org/10.1039/C8TA01237G.
(16) Pool, V. L.; Dou, B.; Campen, D. G. V.; Klein-Stockert, T. R.; Barnes, F. S.; Shaheen, S. E.; Ahmad, M. I.; Hest, M. F. A. M. van; Toney, M. F. Thermal Engineering of FAPbI 3 Perovskite Material via Radiative Thermal Annealing and in Situ XRD. *Nat. Commun.* **2017**, *8* (2968), 14075. https://doi.org/10.1038/ncomms14075.
(17) Soe, C. M. M.; Stoumpos, C. C.; Harutyunyan, B.; Manley, E. F.; Chen, L. X.; Bedzyk, M. J.; Marks, T. J.; Kanatzidis, M. G. Room Temperature Phase Transition in Methylammonium Lead Iodide Perovskite Thin Films Induced by Hydrohalic Acid Additives. *ChemSusChem* **2016**, *9* (18), 2656–2665. https://doi.org/10.1002/cssc.201600879.
(18) Yu, S.; Yan, Y.; Chen, Y.; Chábera, P.; Zheng, K.; Liang, Z. Enabling Room-Temperature Processed Highly Efficient and Stable 2D Ruddlesden–Popper Perovskite Solar Cells with Eliminated Hysteresis by Synergistic Exploitation of

Additives and Solvents. *J. Mater. Chem. A* **2019**, *7* (5), 2015–2021. https://doi.org/10.1039/C8TA09146C.
(19) Sun, C.; Guo, Y.; Fang, B.; Guan, L.; Duan, H.; Chen, Y.; Li, H.; Liu, H. Facile Preparation of High-Quality Perovskites for Efficient Solar Cells via a Fast Conversion of Wet PbI2 Precursor Films. *RSC Adv.* **2017**, *7* (36), 22492–22500. https://doi.org/10.1039/C7RA03066E.
(20) Zhang, H.; Cheng, J.; Li, D.; Lin, F.; Mao, J.; Liang, C.; Jen, A. K.-Y.; Grätzel, M.; Choy, W. C. H. Toward All Room-Temperature, Solution-Processed, High-Performance Planar Perovskite Solar Cells: A New Scheme of Pyridine-Promoted Perovskite Formation. *Adv. Mater.* **2017**, *29* (13), 1604695. https://doi.org/10.1002/adma.201604695.
(21) Liu, D.; Kelly, T. L. Perovskite Solar Cells with a Planar Heterojunction Structure Prepared Using Room-Temperature Solution Processing Techniques. *Nat. Photonics* **2014**, *8* (2), 133–138. https://doi.org/10.1038/nphoton.2013.342.
(22) Matsui, T.; Seo, J.-Y.; Saliba, M.; Zakeeruddin, S. M.; Grätzel, M. Room-Temperature Formation of Highly Crystalline Multication Perovskites for Efficient, Low-Cost Solar Cells. *Adv. Mater.* **2017**, *29* (15), 1606258. https://doi.org/10.1002/adma.201606258.
(23) Ke, W.; Xiao, C.; Wang, C.; Saparov, B.; Duan, H.-S.; Zhao, D.; Xiao, Z.; Schulz, P.; Harvey, S. P.; Liao, W.; Meng, W.; Yu, Y.; Cimaroli, A. J.; Jiang, C.-S.; Zhu, K.; Al-Jassim, M.; Fang, G.; Mitzi, D. B.; Yan, Y. Employing Lead Thiocyanate Additive to Reduce the Hysteresis and Boost the Fill Factor of Planar Perovskite Solar Cells. *Adv. Mater.* **2016**, *28* (26), 5214–5221. https://doi.org/10.1002/adma.201600594.
(24) Byranvand, M. M.; Song, S.; Pyeon, L.; Kang, G.; Lee, G.-Y.; Park, T. Simple Post Annealing-Free Method for Fabricating Uniform, Large Grain-Sized, and Highly Crystalline Perovskite Films. *Nano Energy* **2017**, *34*, 181–187. https://doi.org/10.1016/j.nanoen.2017.02.017.
(25) Han, Q.; Bai, Y.; Liu, J.; Du, K.; Li, T.; Ji, D.; Zhou, Y.; Cao, C.; Shin, D.; Ding, J.; Franklin, A. D.; Glass, J. T.; Hu, J.; Therien, M. J.; Liu, J.; Mitzi, D. B. Additive Engineering for High-Performance Room-Temperature-Processed Perovskite Absorbers with Micron-Size Grains and Microsecond-Range Carrier Lifetimes. *Energy Environ. Sci.* **2017**, *10* (11), 2365–2371. https://doi.org/10.1039/C7EE02272G.
(26) Sun, Y.; Peng, J.; Chen, Y.; Yao, Y.; Liang, Z. Triple-Cation Mixed-Halide Perovskites: Towards Efficient, Annealing-Free and Air-Stable Solar Cells Enabled by $Pb(SCN)_2$ Additive. *Sci. Rep.* **2017**, *7*, 46193. https://doi.org/10.1038/srep46193.
(27) Abdi-Jalebi, M.; Andaji-Garmaroudi, Z.; Pearson, A. J.; Divitini, G.; Cacovich, S.; Philippe, B.; Rensmo, H.; Ducati, C.; Friend, R. H.; Stranks, S. D. Potassium- and Rubidium-Passivated Alloyed Perovskite Films: Optoelectronic Properties and Moisture Stability. *ACS Energy Lett.* **2018**, *3* (11), 2671–2678. https://doi.org/10.1021/acsenergylett.8b01504.
(28) Li, X.; Ibrahim Dar, M.; Yi, C.; Luo, J.; Tschumi, M.; Zakeeruddin, S. M.; Nazeeruddin, M. K.; Han, H.; Grätzel, M. Improved Performance and Stability of Perovskite Solar Cells by Crystal Crosslinking with Alkylphosphonic Acid ω-Ammonium Chlorides. *Nat. Chem.* **2015**, *7* (9), 703–711. https://doi.org/10.1038/nchem.2324.
(29) Wu, Y.; Xie, F.; Chen, H.; Yang, X.; Su, H.; Cai, M.; Zhou, Z.; Noda, T.; Han, L. Thermally Stable MAPbI3 Perovskite Solar Cells with Efficiency of 19.19% and

Area over 1 Cm2 Achieved by Additive Engineering. *Adv. Mater.* **2017**, *29* (28), 1701073. https://doi.org/10.1002/adma.201701073.
(30) Zhao, Y.; Wei, J.; Li, H.; Yan, Y.; Zhou, W.; Yu, D.; Zhao, Q. A Polymer Scaffold for Self-Healing Perovskite Solar Cells. *Nat. Commun.* **2016**, *7* (1), 10228. https://doi.org/10.1038/ncomms10228.
(31) Wang, K.; Liu, C.; Du, P.; Zheng, J.; Gong, X. Bulk Heterojunction Perovskite Hybrid Solar Cells with Large Fill Factor. *Energy Environ. Sci.* **2015**, *8* (4), 1245–1255. https://doi.org/10.1039/C5EE00222B.
(32) Zhao, X.; Yao, C.; Liu, T.; Hamill, J. C.; Ndjawa, G. O. N.; Cheng, G.; Yao, N.; Meng, H.; Loo, Y.-L. Extending the Photovoltaic Response of Perovskite Solar Cells into the Near-Infrared with a Narrow-Bandgap Organic Semiconductor. *Adv. Mater.* **2019**, *31* (49), 1904494. https://doi.org/10.1002/adma.201904494.
(33) Li, S.-S.; Chang, C.-H.; Wang, Y.-C.; Lin, C.-W.; Wang, D.-Y.; Lin, J.-C.; Chen, C.-C.; Sheu, H.-S.; Chia, H.-C.; Wu, W.-R.; Jeng, U.-S.; Liang, C.-T.; Sankar, R.; Chou, F.-C.; Chen, C.-W. Intermixing-Seeded Growth for High-Performance Planar Heterojunction Perovskite Solar Cells Assisted by Precursor-Capped Nanoparticles. *Energy Environ. Sci.* **2016**, *9* (4), 1282–1289. https://doi.org/10.1039/C5EE03229F.
(34) Liang, P.-W.; Liao, C.-Y.; Chueh, C.-C.; Zuo, F.; Williams, S. T.; Xin, X.-K.; Lin, J.; Jen, A. K.-Y. Additive Enhanced Crystallization of Solution-Processed Perovskite for Highly Efficient Planar-Heterojunction Solar Cells. *Adv. Mater.* **2014**, *26* (22), 3748–3754. https://doi.org/10.1002/adma.201400231.
(35) Zhang, W.; Pathak, S.; Sakai, N.; Stergiopoulos, T.; Nayak, P. K.; Noel, N. K.; Haghighirad, A. A.; Burlakov, V. M.; deQuilettes, D. W.; Sadhanala, A.; Li, W.; Wang, L.; Ginger, D. S.; Friend, R. H.; Snaith, H. J. Enhanced Optoelectronic Quality of Perovskite Thin Films with Hypophosphorous Acid for Planar Heterojunction Solar Cells. *Nat. Commun.* **2015**, *6* (1), 10030. https://doi.org/10.1038/ncomms10030.
(36) Li, T.; Pan, Y.; Wang, Z.; Xia, Y.; Chen, Y.; Huang, W. Additive Engineering for Highly Efficient Organic–Inorganic Halide Perovskite Solar Cells: Recent Advances and Perspectives. *J. Mater. Chem. A* **2017**, *5* (25), 12602–12652. https://doi.org/10.1039/C7TA01798G.
(37) Liu, S.; Guan, Y.; Sheng, Y.; Hu, Y.; Rong, Y.; Mei, A.; Han, H. A Review on Additives for Halide Perovskite Solar Cells. *Adv. Energy Mater.* **2020**, *10* (13), 1902492. https://doi.org/10.1002/aenm.201902492.
(38) Roldán-Carmona, C.; Gratia, P.; Zimmermann, I.; Grancini, G.; Gao, P.; Graetzel, M.; Nazeeruddin, M. K. High Efficiency Methylammonium Lead Triiodide Perovskite Solar Cells: The Relevance of Non-Stoichiometric Precursors. *Energy Environ. Sci.* **2015**, *8* (12), 3550–3556. https://doi.org/10.1039/C5EE02555A.
(39) Park, B.; Kedem, N.; Kulbak, M.; Lee, D. Y.; Yang, W. S.; Jeon, N. J.; Seo, J.; Kim, G.; Kim, K. J.; Shin, T. J.; Hodes, G.; Cahen, D.; Seok, S. I. Understanding How Excess Lead Iodide Precursor Improves Halide Perovskite Solar Cell Performance. *Nat. Commun.* **2018**, *9* (7813), 3301. https://doi.org/10.1038/s41467-018-05583-w.
(40) Jacobsson, T. J.; Correa-Baena, J.-P.; Halvani Anaraki, E.; Philippe, B.; Stranks, S. D.; Bouduban, M. E. F.; Tress, W.; Schenk, K.; Teuscher, J.; Moser, J.-E.; Rensmo, H.; Hagfeldt, A. Unreacted PbI2 as a Double-Edged Sword for

Enhancing the Performance of Perovskite Solar Cells. *J. Am. Chem. Soc.* **2016**, *138* (32), 10331–10343. https://doi.org/10.1021/jacs.6b06320.
(41) Ilavsky, J. Nika: Software for Two-Dimensional Data Reduction. *J. Appl. Crystallogr.* **2012**, *45* (2), 324–328. https://doi.org/10.1107/S0021889812004037.
(42) Oosterhout, S. D.; Savikhin, V.; Zhang, J.; Zhang, Y.; Burgers, M. A.; Marder, S. R.; Bazan, G. C.; Toney, M. F. Mixing Behavior in Small Molecule:Fullerene Organic Photovoltaics. *Chem. Mater.* **2017**, *29* (7), 3062–3069. https://doi.org/10.1021/acs.chemmater.7b00067.
(43) Abdelsamie, M.; Xu, J.; Bruening, K.; Tassone, C. J.; Steinrück, H.-G.; Toney, M. F. Impact of Processing on Structural and Compositional Evolution in Mixed Metal Halide Perovskites during Film Formation. *Adv. Funct. Mater.* **2020**, *30* (38), 2001752. https://doi.org/10.1002/adfm.202001752.
(44) Song, T.-B.; Yuan, Z.; Mori, M.; Motiwala, F.; Segev, G.; Masquelier, E.; Stan, C. V.; Slack, J. L.; Tamura, N.; Sutter-Fella, C. M. Revealing the Dynamics of Hybrid Metal Halide Perovskite Formation via Multimodal In Situ Probes. *Adv. Funct. Mater.* **2020**, *30* (6), 1908337. https://doi.org/10.1002/adfm.201908337.
(45) Song, T.-B.; Yuan, Z.; Babbe, F.; Nenon, D. P.; Aydin, E.; De Wolf, S.; Sutter-Fella, C. M. Dynamics of Antisolvent Processed Hybrid Metal Halide Perovskites Studied by In Situ Photoluminescence and Its Influence on Optoelectronic Properties. *ACS Appl. Energy Mater.* **2020**, *3* (3), 2386–2393. https://doi.org/10.1021/acsaem.9b02052.
(46) Mooney, J.; Kambhampati, P. Get the Basics Right: Jacobian Conversion of Wavelength and Energy Scales for Quantitative Analysis of Emission Spectra. *J. Phys. Chem. Lett.* **2013**, *4* (19), 3316–3318. https://doi.org/10.1021/jz401508t.
(47) Guo, Y.; Shoyama, K.; Sato, W.; Matsuo, Y.; Inoue, K.; Harano, K.; Liu, C.; Tanaka, H.; Nakamura, E. Chemical Pathways Connecting Lead(II) Iodide and Perovskite via Polymeric Plumbate(II) Fiber. *J. Am. Chem. Soc.* **2015**, *137* (50), 15907–15914. https://doi.org/10.1021/jacs.5b10599.
(48) Cao, J.; Jing, X.; Yan, J.; Hu, C.; Chen, R.; Yin, J.; Li, J.; Zheng, N. Identifying the Molecular Structures of Intermediates for Optimizing the Fabrication of High-Quality Perovskite Films. *J. Am. Chem. Soc.* **2016**, *138* (31), 9919–9926. https://doi.org/10.1021/jacs.6b04924.
(49) Petrov, A. A.; Sokolova, I. P.; Belich, N. A.; Peters, G. S.; Dorovatovskii, P. V.; Zubavichus, Y. V.; Khrustalev, V. N.; Petrov, A. V.; Grätzel, M.; Goodilin, E. A.; Tarasov, A. B. Crystal Structure of DMF-Intermediate Phases Uncovers the Link Between CH3NH3PbI3 Morphology and Precursor Stoichiometry. *J. Phys. Chem. C* **2017**, *121* (38), 20739–20743. https://doi.org/10.1021/acs.jpcc.7b08468.
(50) Stone, K. H.; Gold-Parker, A.; Pool, V. L.; Unger, E. L.; Bowring, A. R.; McGehee, M. D.; Toney, M. F.; Tassone, C. J. Transformation from Crystalline Precursor to Perovskite in PbCl 2 -Derived MAPbI 3. *Nat. Commun.* **2018**, *9* (1), 3458. https://doi.org/10.1038/s41467-018-05937-4.
(51) Munir, R.; Sheikh, A. D.; Abdelsamie, M.; Hu, H.; Yu, L.; Zhao, K.; Kim, T.; Tall, O. E.; Li, R.; Smilgies, D.-M.; Amassian, A. Hybrid Perovskite Thin-Film Photovoltaics: In Situ Diagnostics and Importance of the Precursor Solvate Phases. *Adv. Mater.* **2017**, *29* (2), 1604113. https://doi.org/10.1002/adma.201604113.
(52) Wang, K.; Tang, M.-C.; Dang, H. X.; Munir, R.; Barrit, D.; Bastiani, M. D.; Aydin, E.; Smilgies, D.-M.; Wolf, S. D.; Amassian, A. Kinetic Stabilization of the Sol–Gel

State in Perovskites Enables Facile Processing of High-Efficiency Solar Cells. *Adv. Mater.* **2019**, *31* (32), 1808357. https://doi.org/10.1002/adma.201808357.
(53) Kerner, R. A.; Zhao, L.; Xiao, Z.; Rand, B. P. Ultrasmooth Metal Halide Perovskite Thin Films via Sol–Gel Processing. *J. Mater. Chem. A* **2016**, *4* (21), 8308–8315. https://doi.org/10.1039/C6TA03092K.
(54) Zhang, H.; Li, D.; Cheng, J.; Lin, F.; Mao, J.; Jen, A. K.-Y.; Grätzel, M.; Choy, W. C. H. Room Temperature Formation of Organic–Inorganic Lead Halide Perovskites: Design of Nanostructured and Highly Reactive Intermediates. *J. Mater. Chem. A* **2017**, *5* (7), 3599–3608. https://doi.org/10.1039/C6TA09845B.
(55) Dutta, N. S.; Noel, N. K.; Arnold, C. B. Crystalline Nature of Colloids in Methylammonium Lead Halide Perovskite Precursor Inks Revealed by Cryo-Electron Microscopy. *J. Phys. Chem. Lett.* **2020**, *11* (15), 5980–5986. https://doi.org/10.1021/acs.jpclett.0c01975.
(56) Pratap, S.; Keller, E.; Müller-Buschbaum, P. Emergence of Lead Halide Perovskite Colloidal Dispersions through Aggregation and Fragmentation: Insights from the Nanoscale to the Mesoscale. *Nanoscale* **2019**, *11* (8), 3495–3499. https://doi.org/10.1039/C8NR09853K.
(57) Wu, Y.; Islam, A.; Yang, X.; Qin, C.; Liu, J.; Zhang, K.; Peng, W.; Han, L. Retarding the Crystallization of PbI2 for Highly Reproducible Planar-Structured Perovskite Solar Cells via Sequential Deposition. *Energy Environ. Sci.* **2014**, *7* (9), 2934–2938. https://doi.org/10.1039/C4EE01624F.
(58) Hu, H.; Singh, M.; Wan, X.; Tang, J.; Chu, C.-W.; Li, G. Nucleation and Crystal Growth Control for Scalable Solution-Processed Organic–Inorganic Hybrid Perovskite Solar Cells. *J. Mater. Chem. A* **2020**, *8* (4), 1578–1603. https://doi.org/10.1039/C9TA11245F.
(59) Lian, X.; Chen, J.; Qin, M.; Zhang, Y.; Tian, S.; Lu, X.; Wu, G.; Chen, H. The Second Spacer Cation Assisted Growth of a 2D Perovskite Film with Oriented Large Grain for Highly Efficient and Stable Solar Cells. *Angew. Chem.* **2019**, *131* (28), 9509–9513. https://doi.org/10.1002/ange.201902959.
(60) Rong, Y.; Venkatesan, S.; Guo, R.; Wang, Y.; Bao, J.; Li, W.; Fan, Z.; Yao, Y. Critical Kinetic Control of Non-Stoichiometric Intermediate Phase Transformation for Efficient Perovskite Solar Cells. *Nanoscale* **2016**, *8* (26), 12892–12899. https://doi.org/10.1039/C6NR00488A.
(61) Do, M.; Kim, I.; Kolaczkowski, M. A.; Kang, J.; Kamat, G. A.; Yuan, Z.; Barchi, N. S.; Wang, L.-W.; Liu, Y.; Jurow, M. J.; Sutter-Fella, C. M. Low-Dimensional Perovskite Nanoplatelet Synthesis Using in Situ Photophysical Monitoring to Establish Controlled Growth. *Nanoscale* **2019**, *11* (37), 17262–17269. https://doi.org/10.1039/C9NR04010B.
(62) S. Parrott, E.; B. Patel, J.; Haghighirad, A.-A.; J. Snaith, H.; B. Johnston, M.; M. Herz, L. Growth Modes and Quantum Confinement in Ultrathin Vapour-Deposited MAPbI 3 Films. *Nanoscale* **2019**, *11* (30), 14276–14284. https://doi.org/10.1039/C9NR04104D.
(63) Franeker, J. J. van; Hendriks, K. H.; Bruijnaers, B. J.; Verhoeven, M. W. G. M.; Wienk, M. M.; Janssen, R. A. J. Monitoring Thermal Annealing of Perovskite Solar Cells with In Situ Photoluminescence. *Adv. Energy Mater.* **2017**, *7* (7), 1601822. https://doi.org/10.1002/aenm.201601822.
(64) Brenes, R.; Eames, C.; Bulović, V.; Islam, M. S.; Stranks, S. D. The Impact of Atmosphere on the Local Luminescence Properties of Metal Halide Perovskite

Grains. *Adv. Mater.* **2018**, *30* (15), 1706208. https://doi.org/10.1002/adma.201706208.
(65) Suchan, K.; Just, J.; Becker, P.; L. Unger, E.; Unold, T. Optical in Situ Monitoring during the Synthesis of Halide Perovskite Solar Cells Reveals Formation Kinetics and Evolution of Optoelectronic Properties. *J. Mater. Chem. A* **2020**, *8* (20), 10439–10449. https://doi.org/10.1039/D0TA01237H.
(66) Demchyshyn, S.; Roemer, J. M.; Groiß, H.; Heilbrunner, H.; Ulbricht, C.; Apaydin, D.; Böhm, A.; Rütt, U.; Bertram, F.; Hesser, G.; Scharber, M. C.; Sariciftci, N. S.; Nickel, B.; Bauer, S.; Głowacki, E. D.; Kaltenbrunner, M. Confining Metal-Halide Perovskites in Nanoporous Thin Films. *Sci. Adv.* **2017**, *3* (8), e1700738. https://doi.org/10.1126/sciadv.1700738.
(67) Malgras, V.; Henzie, J.; Takei, T.; Yamauchi, Y. Hybrid Methylammonium Lead Halide Perovskite Nanocrystals Confined in Gyroidal Silica Templates. *Chem. Commun.* **2017**, *53* (15), 2359–2362. https://doi.org/10.1039/C6CC10245J.
(68) Lee, J.-W.; Lee, D.-K.; Jeong, D.-N.; Park, N.-G. Control of Crystal Growth toward Scalable Fabrication of Perovskite Solar Cells. *Adv. Funct. Mater.* **2019**, *29* (47), 1807047. https://doi.org/10.1002/adfm.201807047.
(69) Son, D.-Y.; Lee, J.-W.; Choi, Y. J.; Jang, I.-H.; Lee, S.; Yoo, P. J.; Shin, H.; Ahn, N.; Choi, M.; Kim, D.; Park, N.-G. Self-Formed Grain Boundary Healing Layer for Highly Efficient CH 3 NH 3 PbI 3 Perovskite Solar Cells. *Nat. Energy* **2016**, *1* (7), 16081. https://doi.org/10.1038/nenergy.2016.81.
(70) Juarez-Perez, E. J.; Hawash, Z.; Raga, S. R.; Ono, L. K.; Qi, Y. Thermal Degradation of CH3NH3PbI3 Perovskite into NH3 and CH3I Gases Observed by Coupled Thermogravimetry–Mass Spectrometry Analysis. *Energy Environ. Sci.* **2016**, *9* (11), 3406–3410. https://doi.org/10.1039/C6EE02016J.

TOC Figure:

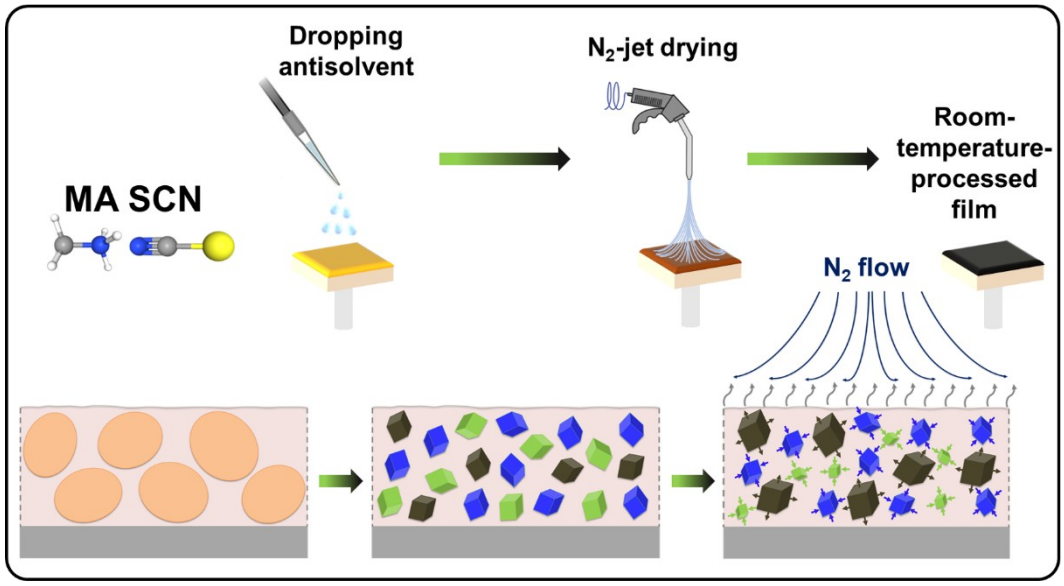
Dropping
antisolvent
N_2-jet drying
Room-
temperature-
processed
film
MA SCN
N_2 flow